Quaternary Geochronology 30 (2015) 114–131

Contents lists available at ScienceDirect

Quaternary Geochronology

journal homepage: www.elsevier.com/locate/quageo

Research paper

A new Holocene eruptive history of Erebus volcano, Antarctica using cosmogenic ^{3}He and ^{36}Cl exposure ages

David E.F. Parmelee [a, *], Philip R. Kyle [a], Mark D. Kurz [b], Shasta M. Marrero [c], Fred M. Phillips [a]

[a] Department of Earth and Environmental Sciences, New Mexico Tech, Socorro, NM 87801, USA
[b] Department of Marine Chemistry and Geochemistry, Woods Hole Oceanographic Institution, Woods Hole, MA, USA
[c] School of GeoSciences, University of Edinburgh, Edinburgh EH8 9XP, UK

ARTICLE INFO

Article history:
Received 27 March 2015
Received in revised form
30 August 2015
Accepted 1 September 2015
Available online 5 September 2015

Keywords:
Erebus volcano
Cosmogenic nuclides
Exposure age
Helium-3
Chlorine-36

ABSTRACT

The ages of recent effusive eruptions on Erebus volcano, Antarctica are poorly known. Published ^{40}Ar/^{39}Ar ages of the 10 youngest "post-caldera" lava flows are unreliable because of the young ages of the flows (<10 ka) and the presence of excess ^{40}Ar. Here we use cosmogenic ^{3}He and ^{36}Cl to provide new ages for the 10 youngest flows and 3 older summit flows, including a newly recognized flow distinguished by its exposure age. Estimated eruption ages of the post-caldera flows, assuming no erosion or prior snow cover, range from 4.52 ± 0.08 ka to 8.50 ± 0.19 ka, using Lifton et al. (2014) to scale cosmogenic production rates. If the older Lal (1991)/Stone (2000) model is used to scale production rates, calculated ages are older by 16–25%. Helium-3 and chlorine-36 exposure ages measured on the same samples show excellent agreement. Helium-3 ages measured on clinopyroxene and olivine from the same samples are discordant, probably due in part to lower-than-expected ^{3}He production rates in the Fe-rich olivine. Close agreement of multiple clinopyroxene ^{3}He ages from each flow indicates that the effects of past snow coverage on the exposure ages have been minimal.

The new cosmogenic ages differ considerably from published ^{40}Ar/^{39}Ar and ^{36}Cl ages and reveal that the post-caldera flows were erupted during relatively brief periods of effusive activity spread over an interval of ~4 ka. The average eruption rate over this interval is estimated to be 0.01 km^{3}/ka. Because the last eruption was at least 4 ka ago, and the longest repose interval between the 10 youngest eruptions is ~1 ka, we consider the most recent period of effusive activity to have ended.

1. Introduction

Erebus volcano is a 3794-m-high polygenetic stratovolcano located on Ross Island in the southern Ross Sea, Antarctica (Fig. 1). As the most active volcano in Antarctica, Erebus is best known for its persistent anorthoclase phonolite lava lake, frequent Strombolian eruptions, and long-term magmatic stability (Kyle et al., 1992; Aster et al., 2003; Oppenheimer and Kyle, 2008; Iverson et al., 2014). Volcanic activity of Erebus spans at least 1.3 Ma, with erupted lavas and tephra ranging in composition from basanite to phonolite (Esser et al., 2004; Kelly et al., 2008b). No eruptions producing lava flows have occurred on Erebus since its discovery in 1841; however, a series of young-looking flows near the summit suggests a period of recent effusive eruptive activity. The ages of these flows are essential for understanding the current constructive phase of Erebus and its potential for future eruptions.

The eruptive history of Erebus volcano has previously been investigated using ^{40}Ar/^{39}Ar geochronology (Esser et al., 2004; Harpel et al., 2004; Kelly et al., 2008a). While ^{40}Ar/^{39}Ar ages have been crucial to developing our understanding of the growth and evolution of Erebus, ages of the youngest flows (<30 ka) are imprecise and potentially inaccurate due to low concentrations of radiogenic ^{40}Ar and high concentrations of magmatic excess ^{40}Ar trapped in melt inclusions (Esser et al., 1997). Precise dating of these flows is important for evaluating the frequency and eruption rates of effusive eruptions on Erebus and determining whether Erebus is still in the midst of an effusive eruptive phase. Young lava flows with excess ^{40}Ar may be more precisely dated using cosmogenic nuclides, which have been used in other studies to date surfaces as young as a few hundred years, if the surfaces of the

* Corresponding author.
E-mail address: davidefparmelee@gmail.com (D.E.F. Parmelee).

http://dx.doi.org/10.1016/j.quageo.2015.09.001

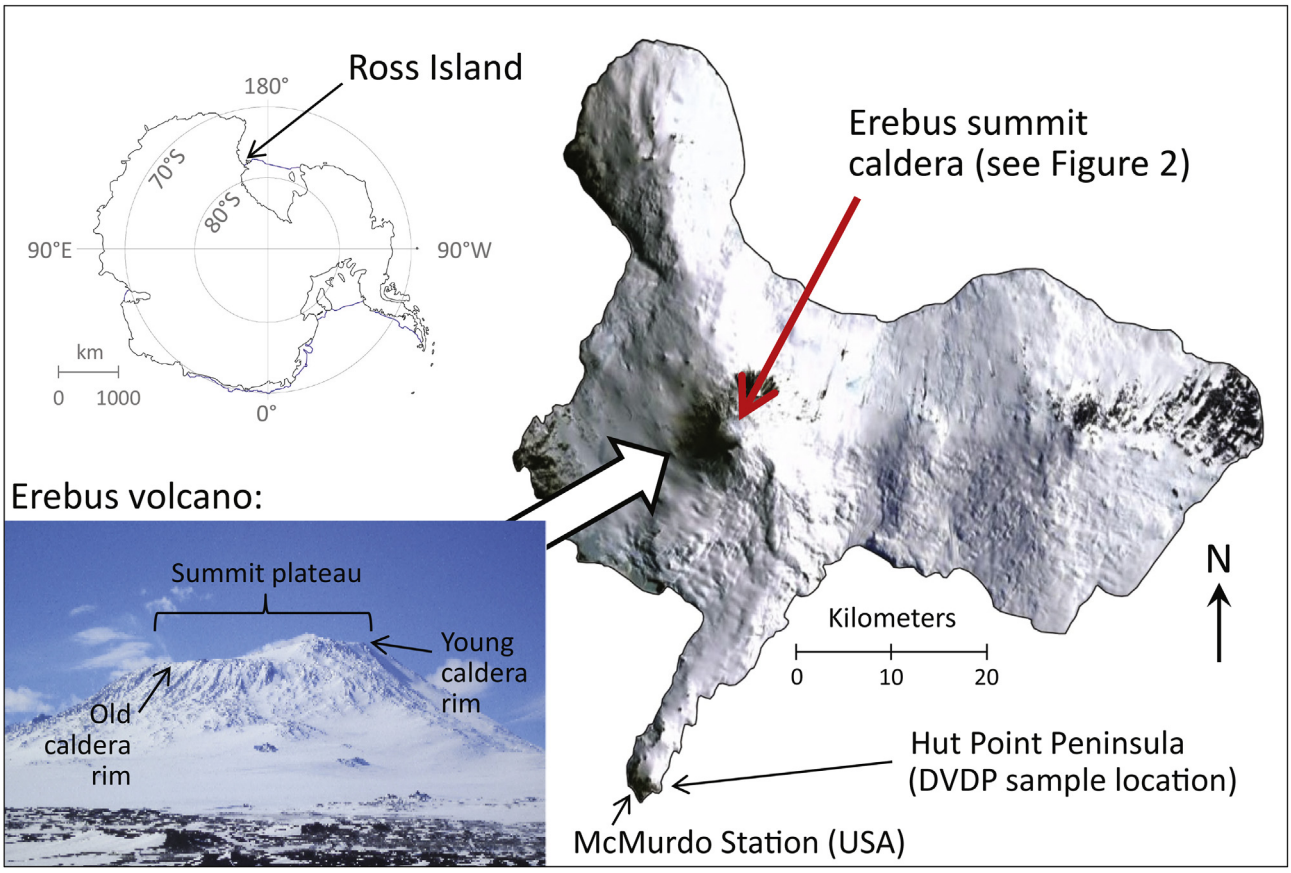

Fig. 1. Location map of Ross Island and profile view of Erebus looking east.

flows have been continuously exposed and experienced minimal erosion since emplacement (e.g., Kurz et al., 1990; Cerling et al., 1999; Licciardi et al., 1999; Hungerford et al., 2002; Fenton and Niedermann, 2014). Erebus is an outstanding location for cosmogenic dating because its high latitude, high elevation, and the anomalously low air pressure over Antarctica (Stone, 2000) result in some of the highest cosmogenic production rates on Earth.

In this paper, we measure cosmogenic ^{3}He in clinopyroxene and olivine and ^{36}Cl in anorthoclase to determine the exposure ages of the youngest lava flows on Erebus volcano. Determining ages using two different nuclides on the same samples permits better assessment of the accuracy of each method and provides a useful comparison of the recently calibrated ^{3}He and ^{36}Cl production rates from Borchers et al. (2015) and Marrero et al. (2015b). These new ages of lava flows previously dated by ^{40}Ar/^{39}Ar and, in some cases, ^{36}Cl in whole rock provide insight into the efficacy of different dating methods for young (<10 ka) rocks. Our results show that the youngest lava flows on Erebus were erupted over a shorter interval than previously thought. We use the new ages to present a revised chronology of recent effusive eruptions and to examine repose rates of the volcanism.

2. Erebus volcano

Erebus volcano lies at the southern end of the Terror Rift, a zone of Late Cenozoic extension and volcanism located near the western margin of the intra-continental West Antarctic Rift System (WARS) (Behrendt, 1999; Hall et al., 2007; Rilling et al., 2009). It is one of ~50 major alkaline, mainly silica-undersaturated volcanoes within the WARS that belong to the McMurdo Volcanic Group (Kyle, 1990). It has been proposed that Erebus and the three other volcanoes on Ross Island (Mt. Terror, Mt. Bird, and Hut Point Peninsula) overlie a mantle hot-spot (Kyle et al., 1992; Behrendt, 1999; Gupta et al., 2009).

Esser et al. (2004) used ^{40}Ar/^{39}Ar ages to examine the history of Erebus. They divide it into three phases: 1) a proto-Erebus shield building phase (1.3–1.0 Ma), during which basanites and tephrites were erupted to form a broad shield volcano; 2) a proto-Erebus cone building phase (1.0 Ma–250 ka), marked by the eruption of more evolved phonotephrites and tephriphonolites to form a more steeply-sloping cone; and 3) the modern Erebus cone building phase (250 ka–present), when anorthoclase-phyric tephriphonolites and phonolites erupted at an increased rate to form most of the upper volcanic structure seen today. Additional ^{40}Ar/^{39}Ar dating by Harpel et al. (2004) and Kelly et al. (2008a) showed that flows have been erupted near the present-day summit of Erebus for at least the last 172 ka, and that for the past 25 ka the summit area has been the exclusive center of activity. Current activity consists of periodic small Strombolian eruptions from a long-lived convecting lava lake in the Main Crater, which can eject lava bombs up to 1 km from the summit (Caldwell and Kyle, 1994; Oppenheimer et al., 2011; Gerst et al., 2013), and rare small phreatic eruptions (Dibble et al., 1994).

The most recent large eruptions on Erebus resulted in the formation of a summit caldera and subsequent infilling of the caldera by anorthoclase-phyric phonolite lava flows, forming a broad, gently sloping plateau. Harpel et al. (2004) proposed that the caldera was formed by at least two distinct episodes of collapse, the

first encompassing most or all of the 4-km-diameter summit plateau and the second overlapping the southwestern portion of the first. $^{40}Ar/^{39}Ar$ ages of flows truncated by the first caldera collapse (referred to as "Old Pre-caldera flows") range from 76 ± 2 ka to 172 ± 5 ka (1σ analytical uncertainty), and ages of flows truncated by the second caldera collapse (referred to as "Young Pre-caldera flows") range from 21 ± 2 ka to 27 ± 2 ka (Harpel et al., 2004; Kelly et al., 2008a).

Mapping of the summit area by Caldwell (1989) and Harpel et al. (2004) based on field observations and aerial photographs has delineated 10 caldera-filling phonolite lava flows, referred to below as the "post-caldera flows" (Fig. 2). Due to extensive snow and ice coverage, the lateral extent of these flows is highly uncertain in many places, particularly in the southern portion of the caldera. The post-caldera flows are petrologically identical, geochemically very similar, and have $^{40}Ar/^{39}Ar$ ages ranging from 0 ± 2 ka to 17 ± 4 ka, with an average interval of 1.8 ka between flows (Harpel et al., 2004; Kelly et al., 2008a). The post-caldera lava flows are the youngest flows on Erebus and the primary focus of this study.

Most of the $^{40}Ar/^{39}Ar$ ages determined on anorthoclase separates from the post-caldera flows have large, overlapping analytical uncertainties due to their young ages, making the timing and sequence of eruptions difficult to interpret. Erebus lavas have also been shown to contain significant quantities of excess ^{40}Ar in anorthoclase-hosted melt inclusions (Esser et al., 1997), meaning that incomplete removal of melt inclusions from the samples prior to irradiation and analysis can result in overestimation of $^{40}Ar/^{39}Ar$ ages. To test the accuracy of the $^{40}Ar/^{39}Ar$ ages, Kelly et al. (2008a) determined ^{36}Cl exposure ages in whole rock samples from three of the post-caldera flows (Lower Ice Tower Ridge, Lower Hut, and Northeast). All three ^{36}Cl ages, as calculated and reported by Kelly et al. (2008a), are significantly more precise and consistently younger than, but within 2σ analytical uncertainty of, the $^{40}Ar/^{39}Ar$ ages reported by Harpel et al. (2004) for the same flows.

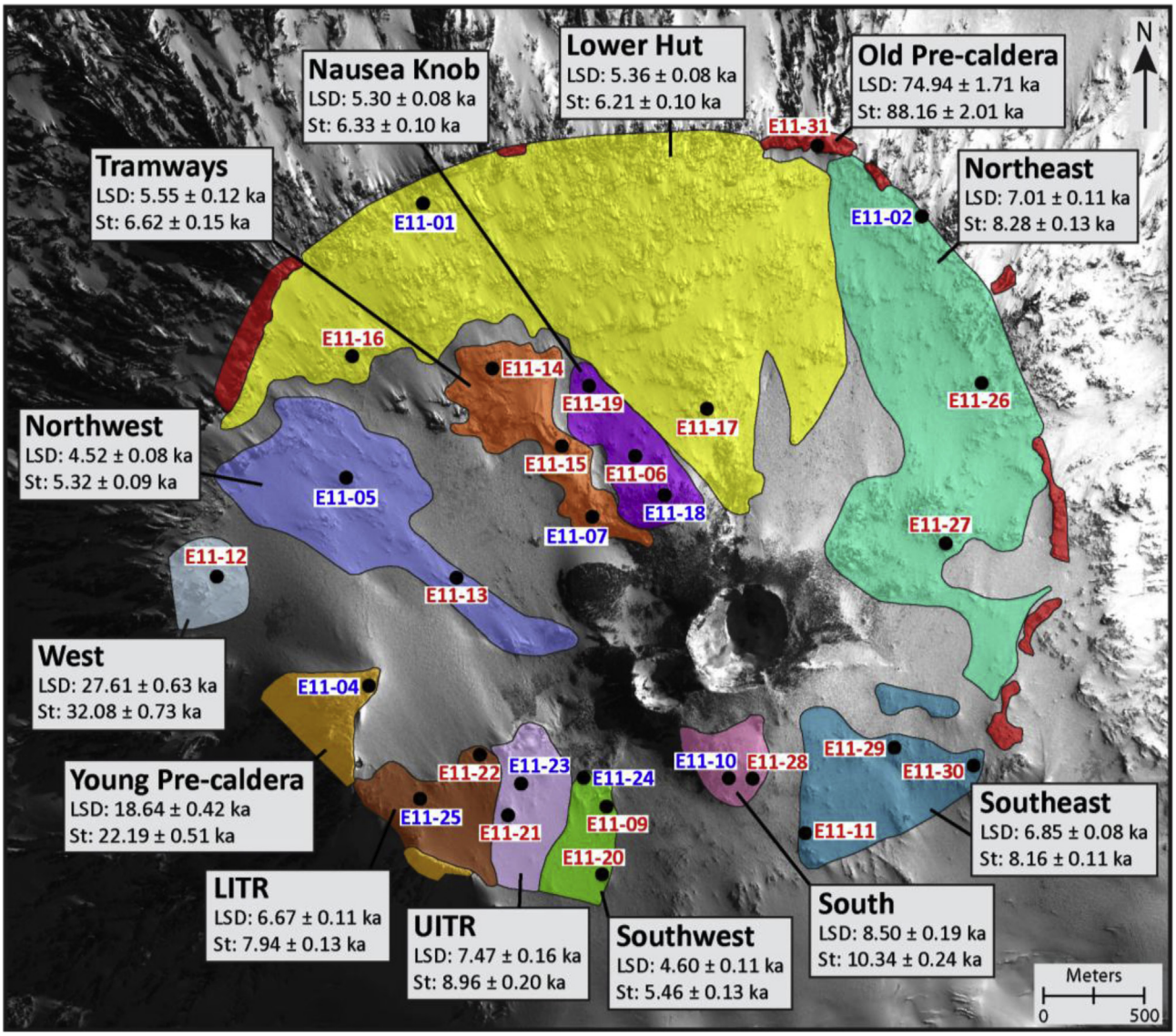

Fig. 2. Map of the Erebus summit caldera lava flows and exposure age sample locations. The lava flows were originally mapped by Caldwell (1989) and Harpel et al. (2004) based on field observations and aerial photographs. All lava flow boundaries are approximate. For each flow, the estimated eruption age and 1σ analytical uncertainty, calculated from clinopyroxene ^{3}He exposure ages as described in the text (section 5.7), is shown using Lifton et al. (2014) (LSD) and Lal (1991)/Stone (2000) (St) production rate scaling. Blue samples are those dated using both ^{3}He and ^{36}Cl and red samples were dated only using ^{3}He. LITR = Lower Ice Tower Ridge, UITR = Upper Ice Tower Ridge. (For interpretation of the references to color in this figure caption, the reader is referred to the web version of this article.)

3. Methods

3.1. Sample collection

Thirty-one exposure age samples were collected from the 10 post-caldera lava flows, an Old Pre-caldera flow, and a Young Pre-caldera flow (Table 1, Fig. 2). Each sample was collected from the top 5 cm of the lava flow. Two samples (E11-03 and E11-08) were later determined to be lava bombs unassociated with any lava flow and are excluded from the remainder of this paper (data for these samples can be found in Supplements A–D). Sample locations were determined using GPS and checked against satellite imagery (Csatho et al., 2008). Replicate samples were taken from different areas of each of the post-caldera flows. Wherever possible, samples were collected from elevated horizontal surfaces to maximize exposure to cosmic rays and minimize the potential for past snow coverage. Surfaces with distinguishable pahoehoe ropes, indicative of minimal erosion, were preferred, though not available at all sample sites. To estimate the effect of shielding of the cosmic ray flux by surrounding topography, the azimuth (relative to true north) and inclination angle of topographic high and low points along the horizon at each sample location, as well as the dip of the sample surface, were measured using a Brunton compass and clinometer. Details of sample locations and other field data are given in Supplement A.

To measure sample bulk densities, a representative section of rock was selected and weighed, then coated in a thin layer of wax to seal vesicles and submerged in a partially-filled volumetric cylinder to determine its volume.

3.2. Helium-3 analysis

Cosmogenic ^{3}He was measured in clinopyroxenes from 31 samples and in olivines from 3 samples (E11-02, E11-05, and E11-31). Whole-rock samples were crushed to <1 mm for a few seconds using a stainless steel TEMA ring and puck mill or <2 mm using a jaw crusher and disk grinder. Samples used for ^{36}Cl analysis were crushed to the smaller grain size, whereas samples used only for ^{3}He analysis were crushed to the larger grain size. High-density minerals, which included clinopyroxene and olivine, were separated from the 0.5–1 or 1–2 mm fraction of each sample using undiluted lithium metatungstate, a heavy liquid with a specific gravity of 2.95. Grains that sank were rinsed with deionized water, acetone, and ethanol (15 min in each solvent in an ultrasonic bath) and air dried at room temperature. Magnetite-rich grains were removed using a hand magnet. Pure clinopyroxene or olivine grains

Table 1
Locations and physical attributes of dated lava flow samples.

Lava flow/Sample ID	Lat. (dec. deg.)	Lon. (dec. deg)	Elev. (m)	Atm. pres. (hPa)	Shielding	$\Lambda_{f,e}$ (g/cm^2)	Thickness (cm)	Bulk dens. (g/cm^3)
Lower Hut								
E11-01	−77.5080	167.0962	3283	629.3	0.997	137.5	1.5	2.2
E11-16	−77.5148	167.0813	3285	629.1	0.999	140.4	2.5	2.0
E11-17	−77.5173	167.1554	3488	611.0	0.998	141.5	4.0	2.0
Lower Ice Tower Ridge								
E11-22	−77.5330	167.1077	3526	607.7	0.999	140.5	2.5	1.9
E11-25	−77.5349	167.0950	3465	613.1	0.999	141.4	2.5	1.5
Nausea Knob								
E11-06	−77.5194	167.1402	3502	609.8	0.992	141.8	4.0	1.5
E11-18	−77.5212	167.1462	3618	599.7	0.999	140.4	2.0	1.4
E11-19	−77.5162	167.1307	3396	619.2	0.996	141.5	3.0	2.2
Northeast								
E11-02	−77.5087	167.2004	3360	622.4	0.998	141.1	3.5	1.9
E11-26	−77.5162	167.2128	3453	614.1	0.999	140.8	2.75	2.0
E11-27	−77.5234	167.2050	3538	606.6	0.999	141.1	2.5	2.0
Northwest								
E11-05	−77.5204	167.0795	3298	627.9	0.999	139.6	3.5	2.0
E11-13	−77.5249	167.1027	3436	615.6	0.996	140.3	2.75	1.9
Old Pre-caldera								
E11-31	−77.5054	167.1785	3365	621.9	0.998	139.1	2.0	1.8
South								
E11-10	−77.5340	167.1597	3653	596.6	0.994	141.3	3.0	1.9
E11-28	−77.5340	167.1647	3633	598.4	0.995	142.2	2.5	1.9
Southeast								
E11-11	−77.5365	167.1755	3502	609.8	0.994	139.5	3.0	1.6
E11-29	−77.5327	167.1944	3519	608.3	0.997	141.2	4.0	2.1
E11-30	−77.5335	167.2109	3458	613.7	0.998	140.4	2.0	1.7
Southwest								
E11-09	−77.5353	167.1343	3544	606.1	0.996	141.3	2.5	1.7
E11-20	−77.5384	167.1332	3447	614.6	0.997	141.0	3.0	1.8
E11-24	−77.5339	167.1292	3558	604.9	0.994	137.3	3.0	1.4
Tramways								
E11-07	−77.5222	167.1313	3534	607.0	0.996	141.8	2.0	1.6
E11-14	−77.5154	167.1104	3372	621.3	0.999	141.2	3.5	1.5
E11-15	−77.5190	167.1249	3453	614.1	0.996	141.6	1.5	2.3
Upper Ice Tower Ridge								
E11-21	−77.5356	167.1135	3510	609.1	0.998	141.0	2.75	2.1
E11-23	−77.5343	167.1164	3535	606.9	0.996	137.1	3.0	1.8
West								
E11-12	−77.5248	167.0527	3199	636.9	0.997	140.1	3.0	1.9
Young Pre-caldera								
E11-04	−77.5298	167.0844	3473	612.4	0.999	140.8	1.5	2.0

$\Lambda_{f,e}$ = effective attenuation length. Atmospheric pressure is calculated based on latitude, longitude, and elevation using the CRONUScalc exposure age calculator (Marrero et al., 2015a), which uses the ERA-40 model of the atmosphere (Uppala et al., 2005).

were handpicked from the nonmagnetic fraction, taking care to avoid grains with adhered matrix glass, visible surface alteration, or a large number of mineral inclusions. Some clinopyroxene grains had a very thin film of glass adhered to the outside that was not removed. Olivine grains, which had larger bits of matrix glass adhered to the outside, were abraded using compressed air to remove the exterior and then rinsed in 10% HNO_3, making the final olivine grain size 0.25–1 mm.

Clinopyroxene and olivine were analyzed for He concentration and isotopic composition at the Woods Hole Oceanographic Institution following previously described methods (e.g., Kurz et al., 1990; Licciardi et al., 1999; Ackert et al., 2003). Helium-3 in the mineral grains comes from both cosmogenic and magmatic sources. The grains were first crushed in a vacuum to selectively release magmatic He, which is contained in melt and fluid inclusions. The released gas was purified by a series of getters and cryogenic traps and measured in a 90° magnetic sector noble gas mass spectrometer. The powdered minerals were then wrapped in aluminum foil and melted in a double-walled resistance furnace to release all remaining He in the grains, which was also purified and measured.

To determine whether the $^3He/^4He$ ratios measured during crushing were offset from the true magmatic value by the release of small amounts of cosmogenic He, 11 olivine separates from hyaloclastite cored by the Dry Valley Drilling Project (DVDP) core 3 (Kyle, 1981) were also crushed and analyzed for He isotopes. DVDP core 3 was drilled at Hut Point Peninsula, an eruptive center on Ross Island located 38 km south-southwest of Erebus's summit (Fig. 1). Though the lavas exposed in the DVDP core erupted from a different vent than the Erebus lavas, we assume their magmatic $^3He/^4He$ ratios are similar because basic lavas throughout Ross Island all share the same radiogenic isotope signature, implying a relatively uniform mantle source for all vents (Sims et al., 2008). Since the DVDP lavas were erupted underwater, the $^3He/^4He$ ratio of the He released from olivine during crushing should be close to the true magmatic value and is not at risk of contamination by cosmogenic $^3He/^4He$.

Helium-3 concentrations were calculated by:

$$^3He_{cosmogenic} = \left[\left(\frac{^3He}{^4He}\right)_{melt} - \left(\frac{^3He}{^4He}\right)_{magmatic}\right] \times {}^4He_{melt}$$

where $\left(\frac{^3He}{^4He}\right)_{melt}$ and $^4He_{melt}$ are the $^3He/^4He$ ratio and concentration of ^4He measured after melting the sample, and $\left(\frac{^3He}{^4He}\right)_{magmatic}$ is the $^3He/^4He$ ratio of mantle-derived He trapped in the sample at the time of eruption. For $\left(\frac{^3He}{^4He}\right)_{magmatic}$, we use the error-weighted mean of the $^3He/^4He$ values measured in the DVDP olivines rather than the $^3He/^4He$ values measured during crushing of each sample (see section 4.1.1). We assume cosmogenic ^4He to be negligible relative to magmatic ^4He, and cosmogenic ^3He produced from thermal neutron capture by ^6Li to be negligible based on the probable low Li concentrations of the clinopyroxene and olivine samples (Brenan et al., 1998; Dunai et al., 2007). Radiogenic ^4He ($^4He_{rad}$) produced post-eruption by the alpha decay of U and Th in the mineral grain, matrix glass, glass inclusions, and apatite inclusions is estimated in Supplement D (section D.2.1). Accounting for $^4He_{rad}$ increases ^3He exposure ages by <1%, significantly less than the 1σ analytical uncertainty of the ages. Corrections for $^4He_{rad}$ are not applied to the results presented below.

Clinopyroxene and olivine grains from each dated sample were analyzed for major element composition using a Cameca SX100 electron microprobe at New Mexico Tech. For each mineral sample, 2–4 points spaced between the core and rim of each grain were analyzed on 4–6 grains.

3.3. Chlorine-36 analysis

Ten samples were analyzed for ^{36}Cl by accelerator mass spectrometer (AMS), including one from each post-caldera lava flow except Southeast Flow and one from the Young Pre-caldera flow. Erebus phonolite is known to have high Cl contents (~1100 ppm; Kelly et al., 2008a), almost all of which is sequestered in matrix glass and melt inclusions. Schimmelpfennig et al. (2009) and Marrero (2012) have suggested that elevated Cl content in a sample may decrease the accuracy of the calculated exposure age due to large uncertainties in the rate of ^{36}Cl production by low-energy neutron capture on ^{35}Cl. To increase the reliability of exposure ages calculated in this study, all ^{36}Cl analyses were made on anorthoclase separates that contained low concentrations of Cl.

Whole rock samples were crushed to a grain size of <1 mm in a TEMA mill. Approximately 50 g of crushed whole rock was powdered and sent to SGS Mineral Services in Toronto, Canada for bulk composition analysis by XRF, ICP-AES, and ICP-MS. The remainder of each sample was sieved to 0.150–1 mm or 0.125–1 mm. Anorthoclase grains were extracted using multiple passes through a Frantz magnetic separator. The anorthoclase was etched in 15% HF for 40 min in an ultrasonic bath to remove chlorine-bearing melt inclusions. Each separate was then leached in 5–12% HNO_3 for 20–72 h and 1% NaOH for 30–60 min to remove meteoric Cl and dissolve surface salts. Approximately 5 g was split from each clean separate, powdered using a mortar and pestle, and sent to Michigan State University for major element analysis by XRF.

Extraction of Cl from anorthoclase separates followed the technique in Marrero (2012), which is modified from Zreda (1994). Approximately 50–60 g of sample was precisely weighed, spiked with ~3 mg of isotopically-enriched chloride (99.66% ^{35}Cl, from ICON), and dissolved in a mixture of HF and HNO_3. Samples were kept on an orbital shaker and monitored for several days. Additional 20 mL aliquots of HF were added periodically until all grains were fully dissolved. $AgNO_3$ was added to the solution to precipitate AgCl, which was then purified by dissolving with NH_4OH and reprecipitating with HNO_3. Sulfur-36, a source of isobaric interference during AMS analysis, was removed by dissolving the AgCl and adding $BaNO_3$ to precipitate $BaSO_4$. AgCl was again precipitated, rinsed, oven-dried, and shipped to PRIME Laboratory at Purdue University for AMS measurement of the $^{35}Cl/^{37}Cl$ and $^{36}Cl/Cl$ ratios.

Three blanks (BS-1, BS-2, and BS-3) were processed for ^{36}Cl analysis alongside the samples. To prepare a blank, ~2 mg of ^{35}Cl spike was mixed with ~150 mL HF and ~25 mL HNO_3. The Cl was then precipitated and purified using the procedure described above and sent for AMS analysis. Chlorine-36 and total Cl concentrations of the anorthoclase separates and blanks were calculated from the AMS results according to the method of Desilets et al. (2006). Calculation details are described in Supplement C.

3.4. Exposure age calculation

Exposure ages were calculated using CRONUScalc (Marrero et al., 2015a), a MATLAB®-based exposure age calculator designed for most commonly used nuclides based on the ^{10}Be–^{26}Al calculator developed by Balco et al. (2008). Globally calibrated production rates from Borchers et al. (2015) and Marrero et al. (2015b) were used for ^3He and ^{36}Cl, respectively (Table 6). Two different methods were used to scale production rates: 1) Lal (1991) as modified by Stone (2000) (here referred to as St), and, 2) the flux-based model presented by Lifton et al. (2014) (referred to as LSD). Atmospheric pressure at the sampling sites based on the ERA-40

model of the atmosphere (Uppala et al., 2005), the topographic shielding coefficient at the sample location, and the effective attenuation length of the cosmic ray flux at the sample location were calculated from field data using CRONUScalc (Table 1). For ^{36}Cl age calculations, we assume each whole rock sample to have no pore water, and analytical water content is set equal to the measured loss on ignition at 1000 °C (LOI) (Table 5). Nucleogenic ^{36}Cl is assumed to be in secular equilibrium with U and Th in the whole rock and subtracted from the measured ^{36}Cl concentration accordingly.

Exposure ages were calculated assuming no erosion or past snow coverage of the sample surface (discussed in section 5.4).

4. Results

4.1. Helium-3 concentration

Measured cosmogenic ^{3}He concentrations in clinopyroxene and olivine are presented in Table 2. Helium-3 concentrations were corrected for the magmatic component using the average ^{3}He/^{4}He ratio measured in the DVDP olivines, as explained below.

4.1.1. Magmatic ^{3}He/^{4}He

In many ^{3}He exposure age and production-rate studies, crushing clinopyroxene or olivine grains has been shown or assumed to quantitatively release only magmatic He (e.g., Kurz, 1986; Kurz et al., 1990; Ackert et al., 2003; Licciardi et al., 1999, 2006; Anslow et al., 2010). In this study, ^{3}He/^{4}He values measured during crushing of exposure age samples varied widely, ranging from 2.42R_a to 22.31R_a, where R_a is the atmospheric ^{3}He/^{4}He ratio (1.384×10^{-6}) (Fig. 3; tabulated results are in Supplement C). Given the relatively small time span and geographical area over which the samples were erupted, it is unlikely that the wide range of ^{3}He/^{4}He values reflects heterogeneities in the mantle source (e.g., Kurz et al., 2004). The dispersion more likely results from two factors: 1) release of non-negligible amounts of cosmogenic ^{3}He during mineral crushing (increasing ^{3}He/^{4}He), and 2) mixing of magma with atmospheric gases in a shallow magma chamber prior to eruption (decreasing ^{3}He/^{4}He). Crushing of the exposure age samples therefore does not yield a reliable value for the ^{3}He/^{4}He ratio of

Table 2
Helium isotope contents and composition in clinopyroxene and olivine phenocrysts from Erebus lava flow samples.

Lava flow/Sample ID	Grain size (mm)	Composition	Mass (g)	$^4He_{melt}$ (10^{-10} cc/g)	$(^3He/^4He)_{melt}$ (R_a)	^3He_c (10^7 atoms/g)
Lower Hut						
E11-01	0.5–1	$Wo_{47}En_{37}Fs_{17}$	0.30747	10.13 ± 0.15	354.38 ± 5.72	1.31 ± 0.03
E11-16	1–2	$Wo_{46}En_{37}Fs_{17}$	0.28041	9.27 ± 0.14	351.89 ± 5.80	1.19 ± 0.03
E11-17	1–2	$Wo_{47}En_{37}Fs_{16}$	0.26566	13.07 ± 0.20	304.97 ± 4.97	1.45 ± 0.03
Lower Ice Tower Ridge						
E11-22	1–2	$Wo_{47}En_{36}Fs_{17}$	0.28676	17.44 ± 0.26	303.30 ± 4.87	1.92 ± 0.04
E11-25	0.5–1	$Wo_{47}En_{37}Fs_{17}$	0.32345	21.92 ± 0.33	227.96 ± 3.77	1.80 ± 0.04
Nausea Knob						
E11-06	1–2	$Wo_{47}En_{37}Fs_{17}$	0.29250	11.93 ± 0.18	338.99 ± 5.42	1.47 ± 0.03
E11-18	0.5–1	$Wo_{47}En_{37}Fs_{16}$	0.29422	11.27 ± 0.17	388.83 ± 6.31	1.60 ± 0.04
E11-19	1–2	$Wo_{47}En_{37}Fs_{17}$	0.27385	12.22 ± 0.18	292.90 ± 4.94	1.30 ± 0.03
Northeast						
E11-02	0.5–1	$Wo_{47}En_{36}Fs_{17}$	0.29709	20.19 ± 0.30	247.39 ± 4.02	1.81 ± 0.04
E11-02(ol)	0.5–1	$Fo_{51}Fa_{45}Te_3$	0.10971	15.47 ± 0.23	267.94 ± 4.56	1.50 ± 0.03
E11-26	1–2	$Wo_{46}En_{36}Fs_{17}$	0.27388	16.83 ± 0.25	303.55 ± 4.81	1.86 ± 0.04
E11-27	1–2	$Wo_{47}En_{36}Fs_{17}$	0.23616	21.56 ± 0.32	246.05 ± 4.02	1.92 ± 0.04
Northwest						
E11-05	0.5–1	$Wo_{47}En_{37}Fs_{16}$	0.29350	10.24 ± 0.15	290.57 ± 4.82	1.08 ± 0.02
E11-05(ol)	0.5–1	$Fo_{52}Fa_{45}Te_3$	0.11418	38.16 ± 0.57	72.78 ± 1.42	0.94 ± 0.03
E11-13	1–2	$Wo_{47}En_{36}Fs_{17}$	0.21388	13.80 ± 0.21	244.36 ± 4.02	1.22 ± 0.03
Old Pre-caldera						
E11-31	0.5–1	$Wo_{46}En_{38}Fs_{16}$	0.27606	139.86 ± 2.10	375.30 ± 6.17	19.17 ± 0.43
E11-31(ol)	0.5–1	$Fo_{55}Fa_{42}Te_2$	0.10807	105.70 ± 1.59	472.19 ± 7.80	18.30 ± 0.41
South						
E11-10	0.5–1	$Wo_{46}En_{37}Fs_{17}$	0.30601	54.52 ± 0.82	129.01 ± 2.12	2.48 ± 0.06
E11-28	1–2	$Wo_{47}En_{37}Fs_{17}$	0.26070	51.94 ± 0.78	142.12 ± 2.30	2.61 ± 0.06
Southeast						
E11-11	0.5–1	$Wo_{47}En_{37}Fs_{17}$	0.30143	15.47 ± 0.23	340.99 ± 5.60	1.92 ± 0.04
E11-29	1–2	$Wo_{47}En_{36}Fs_{17}$	0.22567	15.34 ± 0.23	344.80 ± 5.78	1.93 ± 0.04
E11-30	1–2	$Wo_{46}En_{37}Fs_{17}$	0.27800	27.63 ± 0.41	186.37 ± 3.02	1.84 ± 0.04
Southwest						
E11-09	1–2	$Wo_{47}En_{37}Fs_{16}$	0.26887	19.66 ± 0.29	174.77 ± 2.89	1.23 ± 0.03
E11-20	1–2	$Wo_{47}En_{37}Fs_{17}$	0.27407	15.51 ± 0.23	221.31 ± 3.67	1.24 ± 0.03
E11-24	0.5–1	$Wo_{47}En_{37}Fs_{16}$	0.29108	14.13 ± 0.21	216.15 ± 3.50	1.10 ± 0.03
Tramways						
E11-07	0.5–1	$Wo_{47}En_{37}Fs_{16}$	0.30029	10.31 ± 0.15	421.53 ± 6.81	1.59 ± 0.04
E11-14	1–2	$Wo_{47}En_{37}Fs_{17}$	0.30658	12.09 ± 0.18	306.16 ± 5.06	1.35 ± 0.03
E11-15	0.5–1	$Wo_{47}En_{37}Fs_{17}$	0.26823	14.01 ± 0.21	257.66 ± 4.20	1.31 ± 0.03
Upper Ice Tower Ridge						
E11-21	1–2	$Wo_{47}En_{36}Fs_{17}$	0.27895	19.40 ± 0.29	298.97 ± 4.84	2.11 ± 0.05
E11-23	0.5–1	$Wo_{47}En_{37}Fs_{17}$	0.30535	20.28 ± 0.30	270.83 ± 4.42	1.99 ± 0.05
West						
E11-12	1–2	$Wo_{46}En_{36}Fs_{18}$	0.24707	49.89 ± 0.75	344.29 ± 5.59	6.26 ± 0.14
Young Pre-caldera						
E11-04	0.5–1	$Wo_{46}En_{35}Fs_{19}$	0.23297	51.71 ± 0.78	275.19 ± 4.54	5.16 ± 0.12

All samples are clinopyroxene except Ell-02(ol), E11-05(ol), and E11-31(ol), which are olivine. All helium data have been corrected for analytical blanks and standards run between samples. Uncertainties are reported at 1σ. $R_a = 1.384 \times 10^{-6}$. Pyroxene end-members: wollastonite (Wo; $Ca_2Si_2O_6$), enstatite (En; $Mg_2Si_2O_6$), Ferrosillite (Fs; $Fe_2Si_2O_6$). Olivine end-members: forsterite (Fo: Mg_2SiO_4), fayalite (Fa; Fe_2SiO_4), tephroite (Te; Mn_2SiO_4).

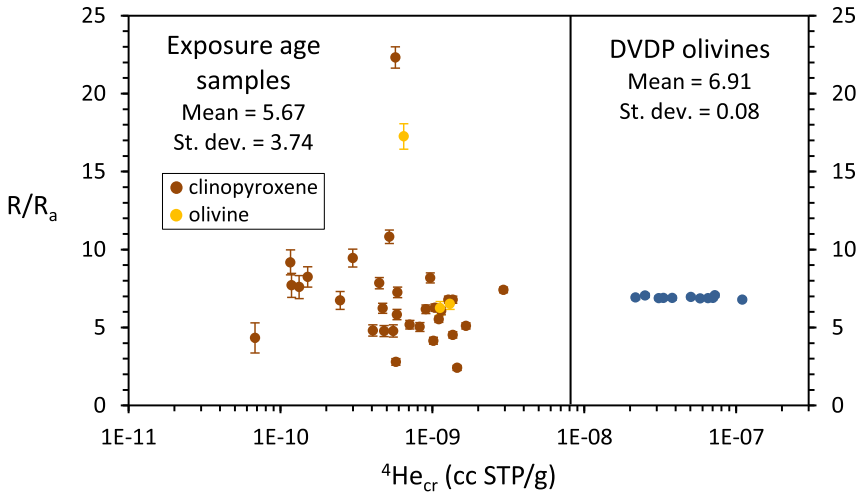

Fig. 3. Helium isotopic composition measured during crushing of exposure age samples (clinopyroxene and olivine) and DVDP olivines. R/R_a is the ratio of $^3He/^4He$ in the sample (R) to $^3He/^4He$ in the atmosphere ($R_a = 1.384 \times 10^{-6}$). $^4He_{cr}$ is the concentration of ^4He released during crushing. Note that the data points with the highest R/R_a are both from sample E11-31, which is from the Old Pre-caldera lava flow sample, the oldest sample in this study. Error bars on data points represent 1σ analytical uncertainty; if no error bars are visible then the uncertainty is smaller than the data symbol. The mean calculated for each dataset is weighted by uncertainty.

mantle-derived helium in this case.

In contrast, $^3He/^4He$ values measured on the DVDP olivine samples cluster tightly between $6.86R_a$ and $7.06R_a$, with an error-weighted mean of $6.91R_a \pm 0.08R_a$ (Fig. 3 and Supplement C). Because the DVDP olivines were rapidly quenched and not exposed to cosmic rays or the atmosphere during or after eruption, their He is derived directly from the Ross Island mantle source. We thus consider the mean DVDP $^3He/^4He$ value the most reliable measure of magmatic $^3He/^4He$ in Erebus lavas and use it to calculate the cosmogenic ^3He concentrations of the exposure age samples.

We recognize it is an assumption that the magmatic $^3He/^4He$ ratio in the DVDP olivines is the same as that in Erebus lavas (see section 3.2); however, the effect of this assumption on the conclusions of this study turns out to be nearly inconsequential. The difference between cosmogenic ^3He concentrations calculated using the mean DVDP $^3He/^4He$ ratio for $\left(\frac{^3He}{^4He}\right)_{magmatic}$ and those calculated using the crushed exposure age sample $^3He/^4He$ ratios for $\left(\frac{^3He}{^4He}\right)_{magmatic}$ is shown in Supplement C to be much smaller than the 1σ analytical uncertainty of either determination for all samples except E11-31.

4.1.2. Clinopyroxene and olivine composition

Clinopyroxene compositions are $Wo_{45-48}En_{35-38}Fs_{15-19}$, and olivine compositions are $Fo_{51-56}Fa_{42-47}Te_{2-3}$ (Table 2). No significant zoning is observed between the cores and rims of the mineral grains. Because compositional variability in terms of the end-members (wollastonite (Wo), enstatite (En), and ferrosilite (Fs) for clinopyroxene, and forsterite (Fo), fayalite (Fa), and tephroite (Te) for olivine) are so low, individual analyses for each sample were averaged to yield the composition given in Table 2 for each sample. Complete electron microprobe analyses are compiled in Supplement B.

4.2. Chlorine-36 concentration

Chlorine-36 and Cl concentrations are presented in Table 3 for anorthoclase samples and Table 4 for blanks. All sample concentrations in Table 3 were blank-corrected for both ^{36}Cl and total Cl according to the method detailed in Supplement C. In applying the corrections, we assume that Cl contamination comes from the HF used to dissolve the samples and ^{36}Cl contamination comes from extraneous particulates inadvertently incorporated into the samples and blanks during AgCl preparation. Exposure ages calculated from uncorrected ^{36}Cl or Cl concentrations would be 0.3–1.3% older or 4.5–7.0% younger, respectively, than those calculated from blank-corrected results. Only ^{36}Cl exposure ages calculated using blank-corrected ^{36}Cl and Cl concentrations are used for discussion below.

4.2.1. Anorthoclase and whole rock composition

The anorthoclase samples have a composition of $An_{12-16}Ab_{67}Or_{17-21}$, similar to the range seen in other studies of Erebus anorthoclase (Kelly et al., 2008b). Concentrations of the major elements in anorthoclase used to calculate the rate of production of ^{36}Cl by spallation and muons (K, Ca, Ti, Fe) are given in Table 5. Whole rock concentrations of major and trace elements used to calculate the rate of production of ^{36}Cl by thermal and epithermal neutron capture and muons are also shown in Table 5. Complete anorthoclase and whole rock analytical results are given in Supplement B.

4.3. Exposure ages

Helium-3 and chlorine-36 exposure ages are presented in Table 7 and displayed graphically in Fig. 4. Ages calculated using the LSD model to scale production rates are referred to as "LSD ages," and those calculated using the St model are referred to as "St ages." Analytical and total uncertainties (1σ) are reported for each age. Analytical age uncertainties account for uncertainties of the nuclide measurements, sample weight (±0.3 mg), sample thickness (±0.25 cm), and bulk density (±0.2 g/cm^3); for ^{36}Cl samples, uncertainties of the ^{35}Cl spike weight (±0.3 mg), HF used for dissolution (±10 mL), ^{35}Cl spike concentration (±0.01 mg ^{35}Cl/g solution), and anorthoclase K_2O, CaO, TiO_2, and Fe_2O_3 concentrations (see Table 5 footnote for specific values) are also included. Total age uncertainties include analytical uncertainty as well as production rate uncertainties (see Table 6 for specific values) and atmospheric pressure uncertainty (5 hPa; Marrero et al., 2015a).

Because the exposure ages in this study are determined on samples of similar chemical composition and from a narrow range

Table 3
Chlorine content and chlorine isotopic composition of anorthoclase from Erebus lava flow samples.

Lava flow/Sample ID	Mass[a] (g)	Spike mass[b] (g)	HF[c] (mL)	$^{35}Cl/^{37}Cl$[d]	$^{36}Cl/10^{15}$ Cl[d]	Cl_{anorth} (ppm)	$^{36}Cl_{anorth}$ (10^5 atoms/g)
Lower Hut							
E11-01	50.7594	3.0114	202	14.446 ± 0.022	466.8 ± 11.0	9.93 ± 0.75	6.38 ± 0.17
Lower Ice Tower Ridge							
E11-25	50.6565	3.0158	175	19.789 ± 0.044	662.9 ± 26.0	4.43 ± 0.69	8.33 ± 0.34
Nausea Knob							
E11-18	59.1791	3.0757	200	9.055 ± 0.019	533.0 ± 14.5	26.25 ± 0.72	7.95 ± 0.23
Northeast							
E11-02	53.5758	3.0072	185	17.752 ± 0.124	672.2 ± 14.4	5.58 ± 0.68	8.18 ± 0.20
Northwest							
E11-05	60.6387	2.0222	207	10.153 ± 0.011	560.4 ± 14.7	9.80 ± 0.63	5.00 ± 0.14
South							
E11-10	52.6520	3.0265	201	13.916 ± 0.015	837.3 ± 26.1	10.75 ± 0.72	11.28 ± 0.37
Southwest							
E11-24	52.3936	3.0026	214	11.292 ± 0.021	360.2 ± 10.6	17.00 ± 0.77	5.23 ± 0.16
Tramways							
E11-07	52.3684	3.0222	215	13.500 ± 0.019	536.3 ± 14.6	10.93 ± 0.75	7.31 ± 0.21
Upper Ice Tower Ridge							
E11-23	49.3166	3.0211	182	12.652 ± 0.021	637.1 ± 16.9	15.62 ± 0.76	9.47 ± 0.27
Young Pre-caldera							
E11-04	59.0636	3.0817	220	17.574 ± 0.010	2102.6 ± 44.8	3.96 ± 0.65	23.98 ± 0.57

All uncertainties are reported at 1σ.
[a] Mass of anorthoclase.
[b] Mass of ^{35}Cl spike added to sample following dissolution. Spike concentration: 0.9999 ± 0.01 mg ^{35}Cl/g solution, $^{35}Cl/Cl = 0.9966$.
[c] Volume of HF used to dissolve anorthoclase phenocrysts.
[d] $^{35}Cl/^{37}Cl$ and $^{36}Cl/10^{15}$ Cl measured in the AgCl target by AMS at PRIME Lab, Purdue University.

Table 4
Chlorine-36 and total Cl concentrations in blanks.

Blank	Spk mass[a] (g)	HF[b] (mL)	$^{35}Cl/^{37}Cl$[c]	$^{36}Cl/10^{15}$ Cl[c]	Cl_{blank} (10^{16} atoms Cl/mL HF)	$^{36}Cl_{blank}$ (10^5 atoms)
BS-1	2.1153	150	16.456 ± 0.070	7.421 ± 2.032	*7.10 ± 0.48*	*3.50 ± 0.96*
BS-2	2.0574	150	29.468 ± 0.242	144.2 ± 11.6	*3.33 ± 0.23*	58.45 ± 4.75
BS-3	2.1167	150	28.325 ± 0.121	6.624 ± 2.073	*3.60 ± 0.24*	*2.78 ± 0.87*
Average[d]					**4.67 ± 0.20**	**3.14 ± 0.65**

All uncertainties are reported at 1σ.
[a] Mass of ^{35}Cl spike used to prepare the blank. 0.9999 ± 0.01 mg ^{35}Cl/g solution, $^{35}Cl/Cl = 0.9966$.
[b] Volume of HF used to prepare the blank.
[c] $^{35}Cl/^{37}Cl$ and $^{36}Cl/10^{15}$ Cl measured in the AgCl target by AMS at PRIME Lab.
[d] Averages are calculated from the *italicized* values. BS-2 is excluded from the $^{36}Cl_{blank}$ average because its ^{36}Cl concentration is an order of magnitude higher than BS-1 and BS-3 as well as previous blanks processed in the same lab by the same procedure.

of elevations, the additional uncertainties incorporated in the total age uncertainty are systematic within the sample set and therefore not relevant for evaluating the relative ages of lava flows and samples (Balco et al., 2008). For most of the discussion below only analytical age uncertainties are used. Total age uncertainties are used for comparison of exposure ages from this study to $^{40}Ar/^{39}Ar$ ages from Harpel et al. (2004) and Kelly et al. (2008a) (section 5.5), and whole-rock ^{36}Cl ages from Kelly et al. (2008a) (section 5.6).

5. Discussion

5.1. LSD vs. St ages

One of the largest sources of potential error in determining exposure ages comes from scaling cosmogenic nuclide production rates. Scaling uncertainty is not well constrained but may be represented by the difference between ages calculated using different scaling models. In this study, St ages are 16–22% older than LSD ages for ^{3}He samples and 20–25% older than LSD ages for ^{36}Cl samples (Table 7).

The large difference between LSD and St ages results primarily from two significant differences between the scaling models. First, the LSD model predicts a faster increase in the strength of the cosmic-ray flux with increasing altitude (Lifton et al., 2014), meaning larger scaling factors than the St model at high elevation. Second, the LSD model accounts for temporal variability in the solar modulation of cosmic rays whereas the St model does not. The effects of solar modulation on cosmic rays are especially large at high latitudes, where the portion of the primary cosmic-ray flux most affected by variations in the solar wind is not moderated by the geomagnetic field (Niedermann, 2002; Lifton et al., 2005). Because the mean solar modulation potential over the past several decades has been higher than during most of the Holocene (Usoskin et al., 2007; Steinhilber et al., 2008), scaling models that do not account for temporal variability of solar modulation may overestimate the ages of high latitude samples.

Scaling uncertainty is systematic amongst samples from similar latitudes and elevations, such as those in this study, and can be excluded when comparing ages of the samples to each other (Balco et al., 2008). For comparison of exposure ages with ages measured by other methods or with other exposure ages measured in a different location, scaling uncertainty is an important consideration that should be taken into account. The large difference between LSD and St ages in this study demonstrates that while exposure ages determined for samples at high latitude and high elevation may be precise as relative ages, their uncertainties are much larger when used as absolute ages.

Despite the large difference between LSD and St ages, the

Table 5
Bulk rock and anorthoclase composition of ^{36}Cl samples. Only elements used to compute the ^{36}Cl production rate are shown.

Lava flow:	Lower Hut	LITR	Nausea Knob	Northeast	Northwest	South	Southwest	Tramways	UITR	Young Pre-caldera
Sample ID:	E11-01	E11-25	E11-18	E11-02	E11-05	E11-10	E11-24	E11-07	E11-23	E11-04
Whole rock (XRF, ICP-AES, ICP-MS)										
SiO_2 (wt %)	55.4	55.2	53.0	54.9	54.8	55.3	55.0	54.5	55.8	55.9
TiO_2	1.03	1.05	1.06	1.08	0.99	1.04	1.06	1.03	1.02	0.98
Al_2O_3	19.7	19.5	19.2	19.5	19.8	19.3	19.5	19.6	19.4	18.9
Fe_2O_3*	5.56	5.80	5.79	5.80	5.38	5.89	5.73	5.64	5.65	6.14
MnO	0.20	0.22	0.19	0.22	0.20	0.22	0.23	0.2	0.21	0.24
MgO	1.00	1.02	0.98	1.03	0.92	1.00	1.02	0.97	0.96	0.90
CaO	2.79	2.81	2.64	2.80	2.81	2.63	2.75	2.75	2.75	2.51
Na_2O	8.34	8.31	8.12	8.36	8.45	8.21	8.24	8.21	8.23	8.34
K_2O	4.50	4.55	4.37	4.48	4.44	4.54	4.51	4.39	4.53	4.67
P_2O_5	0.45	0.46	0.48	0.47	0.43	0.44	0.44	0.46	0.44	0.43
LOI	1.09	0.79	5.49	1.25	1.26	0.88	0.86	2.19	0.44	0.74
Total	100.06	99.71	101.32	99.89	99.48	99.45	99.34	99.94	99.43	99.75
Li (ppm)	20	20	20	20	20	20	20	20	20	20
Be	8	9	8	8	8	8	9	8	8	8
B	<10	<10	<10	<10	<10	<10	<10	<10	<10	<10
Cl[a]	1082	1082	1082	1082	1082	1082	1082	1082	1082	1082
Cr	30	30	30	30	20	20	30	30	30	30
Sm	14.3	15.8	14.3	15.2	14.4	15.5	14.5	14.0	15.4	16.8
Gd	11.5	12.3	11.3	12.0	11.3	12.4	11.9	11.5	12.4	13.4
Th	20.9	21.9	21.4	21.2	21.2	21.4	22.4	21.2	22.2	20.7
U	6.24	6.43	6.88	6.28	6.12	6.63	6.70	6.49	6.49	6.04
Anorthoclase (XRF)[b]										
TiO_2 (wt %)	0.13	0.12	0.13	0.12	0.13	0.13	0.13	0.13	0.12	0.12
Fe_2O_3*	0.42	0.35	0.36	0.32	0.37	0.35	0.38	0.39	0.36	0.34
CaO	3.22	2.95	3.13	2.92	3.25	2.79	3.28	3.17	2.87	2.48
K_2O	3.02	3.24	3.04	3.21	3.01	3.39	2.94	3.03	3.23	3.61

LITR = Lower Ice Tower Ridge. UITR=Upper Ice Tower Ridge. * Total Fe reported as Fe_2O_3. LOI = loss on ignition. A complete list of whole rock major and trace element analyses and anorthoclase major element analyses can be found in Supplement B.

[a] Whole rock Cl is the average of three measurements from Lower Ice Tower Ridge flow (1058 ppm), Lower Hut flow (1085 ppm), and Northeast flow (1104 ppm) from Kelly et al. (2008a).

[b] 1σ uncertainties of XRF analyses on anorthoclase are 0.01 wt% for K_2O, 0.06 wt% for CaO, 0.01 wt % for TiO_2, and 0.05 wt% for Fe_2O_3*. Uncertainties are determined as the standard deviation of replicate measurements on basalt standard BHVO-1 (n = 4) for CaO, TiO_2, and Fe_2O_3* and rhyolite standard RGM-1 (n = 3) for K_2O.

conclusions of this study are essentially the same using either scaling model. For the sake of simplicity and readability, only LSD ages will be used for the remainder of the discussion except where otherwise noted.

5.2. ^{3}He vs. ^{36}Cl ages

Calculated ^{3}He ages in clinopyroxene and ^{36}Cl ages in anorthoclase agree within 1σ analytical error for all samples except E11-10, in which ages agree within 2σ (Table 7; Figs. 4 and 5). The excellent agreement between the ^{3}He and ^{36}Cl ages implies that significant contamination or loss of ^{3}He or ^{36}Cl from the samples before or during analysis is unlikely and the methods used here are robust. More significantly, it implies that the production rates used in this study (Table 6) are internally consistent for the latitude (~77°S) and altitude (~3200–3650 m asl) of the study area.

For ^{36}Cl, this conclusion only applies to the production rates of the pathways that are dominant in the anorthoclase samples, i.e., spallation of K and Ca. Chlorine-36 produced by other pathways, including spallation of Fe and Ti, low-energy neutron absorption, and slow muon capture, constitutes a relatively small portion of the total ^{36}Cl content of these samples. As such, the concordance of ^{3}He and ^{36}Cl ages in this study says little about the accuracy of the production rates determined for these pathways.

5.3. ^{3}He production in Fe-rich olivine

For the three samples (E11-02, E11-05, E11-31) in which ^{3}He was measured in both clinopyroxene and olivine, the cosmogenic ^{3}He concentration in olivine is significantly lower (by 16.8%, 13.5%, and 4.6%, respectively) than that in clinopyroxene, resulting in younger ages being determined in olivine. The difference between cosmogenic ^{3}He concentrations in olivine and those in clinopyroxene is greater than 1σ analytical uncertainty for all three samples and greater than 2σ for E11-02 and E11-05 (Table 2).

These differences probably arise at least in part from the compositional dependence of cosmogenic ^{3}He production. Theoretical estimates from several studies (Lal, 1991; Masarik and Reedy, 1995; Masarik and Beer, 1999; Masarik, 2002) suggest that the production rate of ^{3}He by spallation of Fe and Ca is significantly less than that from Mg, Si, O, and Al. Olivine or pyroxene that is Fe- or Ca-rich should therefore accumulate less ^{3}He over a given time span than more Mg-rich phases. The olivines in this study have nearly twice as much Fe as Mg by weight (see Supplement B). Using the elemental production rates from Masarik (2002) and the average major element composition of each sample, the production rates of ^{3}He in olivine phenocrysts from E11-02, E11-05, and E11-31 are predicted to be, respectively, 7.3%, 6.5%, and 5.4% lower than in clinopyroxene phenocrysts from the same samples (Table 8). The measured differences between ^{3}He concentrations in olivine and clinopyroxene are noticeably larger than this for E11-02 and E11-05; however, the general trend of lower $^{3}He_c$ concentrations in olivine is consistent with these predictions.

The ^{3}He production rate from Borchers et al. (2015) that was used to calculate ages in this study was calibrated from a dataset that included measurements in both olivine and pyroxene (note that this dataset is a subset of the data used by Goehring et al. (2010), with the remainder used for calibration verification). The compositions of the clinopyroxenes in this study ($Wo_{45-48}En_{35-38}Fs_{15-19}$) are similar to those in the calibration dataset ($Wo_{45-50}En_{38-41}Fs_{11-14}$), but the olivines in this study (Fo_{51-56}) are significantly more Fe-rich than those used for calibration (Fo_{75-89}).

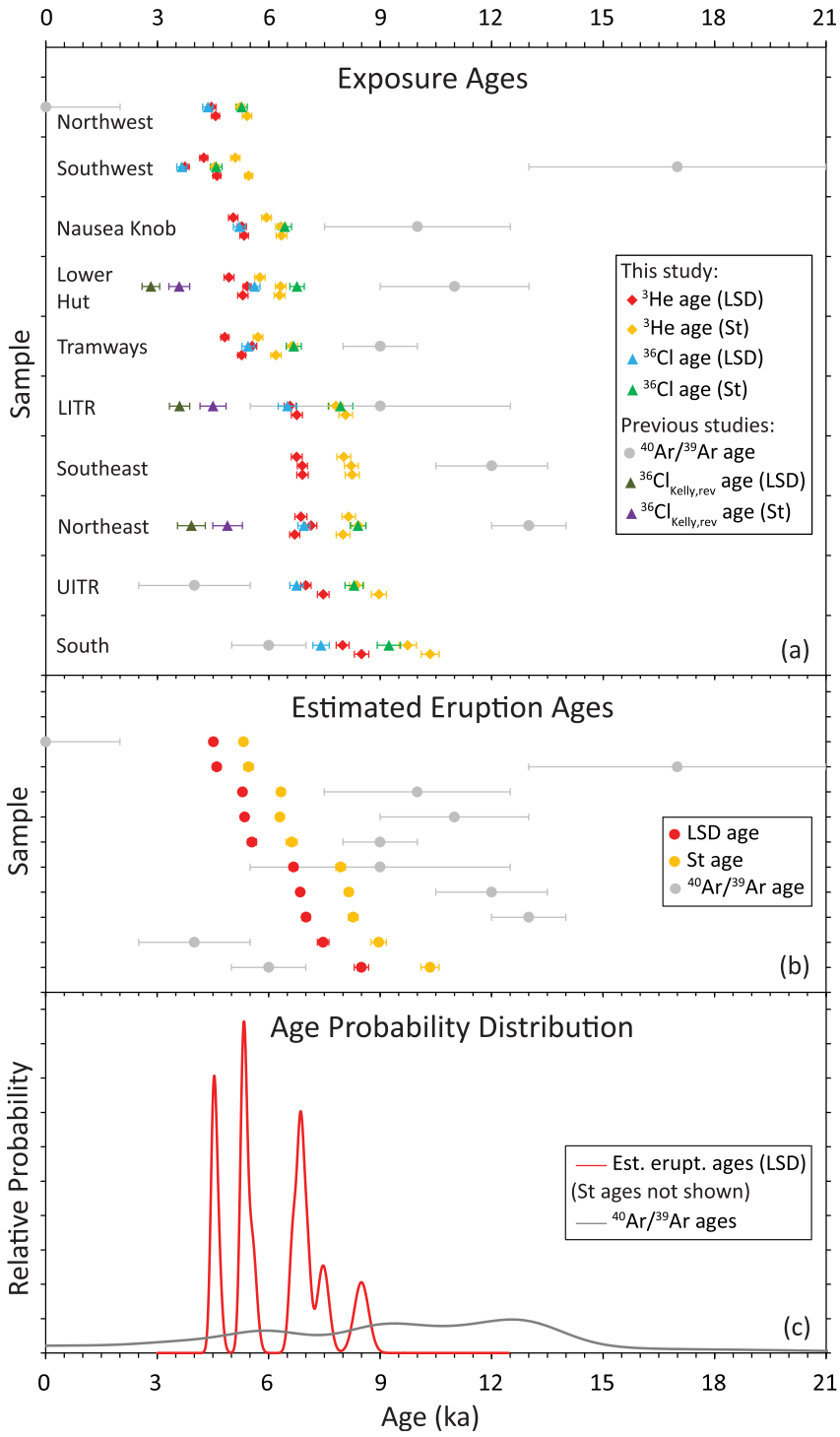

Fig. 4. (a) Clinopyroxene ^{3}He and anorthoclase ^{36}Cl exposure ages for the post-caldera lava flows. Published ^{40}Ar/^{39}Ar ages from Harpel et al. (2004) and Kelly et al. (2008a) and ^{36}Cl ages from Kelly et al. (2008a) are also shown for comparison. Olivine ^{3}He ages are not shown. Error bars represent 1σ analytical uncertainty. LSD ages are calculated using the production rate scaling model of Lifton et al. (2014) and St ages are calculated using Lal (1991)/Stone (2000) scaling. The ^{36}Cl ages from Kelly et al. (2008a) have been recalculated using the same procedure and scaling models used for samples from this study (see section 5.6). (b) Estimated eruption ages, calculated as the error-weighted mean of the oldest clinopyroxene ^{3}He ages from each flow that are concordant within 1σ analytical uncertainty. (c) Age probability distributions of the post-caldera flows based on their estimated eruption ages (LSD only) and ^{40}Ar/^{39}Ar ages using 1σ analytical uncertainty. The distribution represents the relative probability that an effusive eruption occurred within the Erebus caldera at a given point in time. The curve generated by the new exposure ages is much different than that based on published ^{40}Ar/^{39}Ar ages. Whereas the ^{40}Ar/^{39}Ar-based curve suggests an approximately equal, but low, probability of eruptions at any time over the past ~15 ka, the exposure age-based curve indicates a relative high probability of eruptions during short intervals between ~4 and 8 ka. The probability distribution of St ages (not shown) has a similar shape to that of LSD ages but is ~20% older. Either exposure age distribution suggests that the period of heightened effusive activity during which the post-caldera flows erupted has stalled or ended.

Table 6
Published production rates used to calculate exposure ages in this study. All production rates are for sea level, high latitude, and a sample depth of zero.

	LSD scaling	St scaling
^{3}He production rates[a]		
$P_{sp}(0)$	119 ± 19	118 ± 18
^{36}Cl production rates[b]		
$P_{sp,K}(0)$	155 ± 13	151 ± 10
$P_{sp,Ca}(0)$	56.6 ± 4.7	52.5 ± 3.6
$P_{sp,Ti}(0)$	13 ± 3	13 ± 3
$P_{sp,Fe}(0)$	1.9 ± 0	1.9 ± 0
$P_{f}(0)$	690 ± 181	649 ± 201

LSD = Flux-based version of Lifton et al. (2014) scaling model, St = Lal (1991)/Stone (2000) scaling model. Uncertainties are 1σ.

[a] $P_{sp}(0)$ is the production rate of ^{3}He in olivine and pyroxene by spallation of all nuclides heavier than ^{3}He. Production rates are from Borchers et al. (2015) and uncertainties are from Phillips et al. (2015).

[b] $P_{sp,K}(0)$ is the production rate of ^{36}Cl by spallation of K (Marrero et al., 2015b); $P_{sp,Ca}(0)$ is the production rate of ^{36}Cl by spallation of Ca (Marrero et al., 2015b); $Psp,T_i(0)$ is the production rate of ^{36}Cl by spallation of Ti (Fink et al., 2000); $P_{sp,Fe}(0)$ is the production rate of ^{36}Cl by spallation of Fe (Stone, 2005); $P_{f}(0)$ is the production rate of epithermal neutrons from fast neutrons in the atmosphere at the rock surface, which is used to calculate the production rate of ^{36}Cl by low-energy neutron capture (Marrero et al., 2015b).

Helium-3 exposure ages calculated using the Borchers et al. (2015) ^{3}He production rate (115 atoms/g/a using LSD scaling) should therefore be more accurate in this study for clinopyroxene than for olivine. This is supported by concordance of clinopyroxene ^{3}He ages with ^{36}Cl ages in E11-02 and E11-05 (^{36}Cl was not measured in E11-31). Only ^{3}He ages determined in clinopyroxene will be used for the remainder of the discussion.

5.4. Effects of erosion and snow cover

The largest source of uncertainty in the relative ages of the samples comes from geological variables that cannot be constrained, the most important of which are erosion and past snow coverage. Both factors can lead to underestimation of the exposure age – erosion by removing cosmogenic nuclides that have accumulated at the surface, and snow coverage by partially or completely shielding the surface from the cosmic-ray flux.

The degree to which apparent exposure ages are underestimated due to erosion depends on the erosion rate and exposure age of the sample. On Erebus, erosion rates of lava flows are low due to the cold, dry climate and high altitude. If we assume that samples from the post-caldera flows have eroded at a rate of 1 mm/ka for the duration of their exposure, their calculated ^{3}He and ^{36}Cl ages increase by only 0.1–0.6% and 0–0.4%, respectively (Fig. 6). For such young samples on Erebus, the effect of erosion on exposure age is probably negligible.

Exposure ages of the three older samples have greater potential to be influenced by erosion: assuming an erosion rate of 1 mm/ka, the ^{3}He ages of samples E11-04 (18.64 ka), E11-12 (27.61 ka), and E11-31 (74.94 ka) increase by 1.4%, 1.9%, and 5.2%, respectively, and the ^{36}Cl age of E11-04 (17.95 ka) increases by 1.2% (^{36}Cl was not measured in E11-12 or E11-31). The surface of E11-31 appeared noticeably eroded in the field (see Supplement A field notes), meaning the exposure age of E11-31 is probably underestimated. The surfaces of E11-04 and E11-12 had a much fresher appearance with no obvious signs of erosion.

Given the polar, high altitude location of the Erebus summit plateau, snow coverage is the most likely source of potential age underestimation on Erebus for all samples except E11-31, which is more likely to be underestimated due to erosion. The magnitude of the effect of snow coverage on exposure age is a function of the depth, density, and duration of snow cover and does not depend on the age. For example, assuming in the age calculation that the Erebus samples were covered by 1 m of snow with a density of 0.5 g/cm^{3} for 50% of the duration of their exposure would increase their ^{3}He and ^{36}Cl exposure ages by 15–20% based on snow-cover corrections from Gosse and Phillips (2001) and Zweck et al. (2013), regardless of age (Fig. 6).

The degree to which exposure ages have been underestimated due to past snow coverage can be qualitatively evaluated by comparing the ages of samples collected from different areas of the same flow. Because snow cover on the Erebus summit plateau occurs in the form of localized drifts rather than seasonal snowfall, the depth and duration of past snow cover is unlikely to have been uniform from one sample location to the next. Significant burial effects on the cosmogenic nuclide concentrations of surface samples would result in a broad scattering of ages in samples collected from different parts of the same flow.

For lava flows in which multiple samples were collected, we find generally close agreement of ^{3}He ages determined in different areas of the same flow (^{36}Cl ages were determined in only one location per flow and so cannot be compared). The difference between the oldest and youngest ^{3}He age in each flow ranges from 2.2% to 18.6% relative to the oldest, with a median value of 6.1%. In 7 of the 10 post-caldera flows, all ^{3}He exposure ages determined with the same flow have overlapping 2σ analytical uncertainties, and in all 10 post-caldera flows at least 2 ages overlap within 2σ. The narrow age range observed within most of the flows indicates that the effect of snow cover on exposure ages, while not negligible, has been small.

The Southwest and Tramways flows have significantly greater differences between the youngest and oldest exposure ages than the other flows (18.7% and 13.2%, respectively). In the Southwest flow, the only outcrops available for sampling are low-lying, making snow coverage a good explanation for the age range. In the Tramways flow, all three samples were collected from high-standing outcrops not likely to have experienced significant snow cover. The scatter in this case may be the result of surface shift, as both of the Tramways samples with younger apparent ages (E11-14 and E11-15) were collected from detached blocks that may have been rotated sometime after flow emplacement (see field notes in Supplement A). Another possible explanation for the broader age scatter is that the Southwest and/or Tramways lava flow boundaries are mapped incorrectly, in which case the variation in exposure ages could reflect actual differences in the eruption ages of the outcrops from which the samples were collected.

5.5. Comparison of new exposure ages and published ^{40}Ar/^{39}Ar ages

All 10 post-caldera flows as well as the Old Pre-caldera and Young Pre-caldera flows have been dated in prior studies using the ^{40}Ar/^{39}Ar technique (Harpel et al., 2004; Kelly et al., 2008a). Analytical uncertainties (1σ) of the ^{3}He ages (2.0–3.0%) and ^{36}Cl ages (2.3–3.9%) from this study are much smaller than those of published ^{40}Ar/^{39}Ar ages (8–39%), yielding much more reliable relative ages of the flows. The sequence of post-caldera eruptions revealed by the exposure ages differs considerably from that suggested by the ^{40}Ar/^{39}Ar ages (referred to below as “Ar ages”). For instance, the Southwest flow has the oldest Ar age and the youngest exposure ages, and the Upper Ice Tower Ridge flow has the second youngest Ar age and second oldest exposure ages. The span of post-caldera lava flow ages is also quite different: the oldest and youngest Ar ages of the post-caldera flows are 17 ka apart, whereas the difference between the oldest and youngest exposure ages is only 4.7 ka.

To determine which lava flows have concordant exposure ages and Ar ages, we use the total rather than analytical uncertainties of

Table 7
Comparison of new ^{3}He and ^{36}Cl ages on lava flows from Erebus volcano with previously published ^{40}Ar/^{39}Ar and ^{36}Cl ages. All ages are in ka.

Lava flow/ Sample ID	^{3}He		^{36}Cl		^{40}Ar/^{39}Ar[c]
	LSD age[a]	St age[b]	LSD age[a]	St age[b]	Age
Northwest					
E11-05	*4.46 ± 0.11 (0.80)*	*5.23 ± 0.12 (0.82)*	4.36 ± 0.14 (0.35)	5.27 ± 0.16 (0.36)	–
E11-05(ol)	3.82 ± 0.11 (0.64)	4.53 ± 0.12 (0.71)	–	–	–
E11-13	*4.57 ± 0.11 (0.80)*	*5.42 ± 0.12 (0.85)*	–	–	–
Est. Erupt. age	**4.52 ± 0.08 (0.80)**	**5.32 ± 0.09 (0.83)**	–	–	–
Prev. studies	–	–	–	–	0 ± 2
Southwest					
E11-09	4.25 ± 0.12 (0.74)	5.10 ± 0.12 (0.80)	–	–	–
E11-20	*4.60 ± 0.11 (0.84)*	*5.46 ± 0.13 (0.85)*	–	–	–
E11-24	3.75 ± 0.11 (0.68)	4.55 ± 0.10 (0.71)	3.66 ± 0.14 (0.30)	4.59 ± 0.15 (0.32)	–
Est. erupt. age	**4.60 ± 0.11 (0.84)**	**5.46 ± 0.13 (0.85)**	–	–	–
Prev. studies	–	–	–	–	17 ± 4
Nausea Knob					
E11-06	*5.34 ± 0.14 (0.82)*	*6.34 ± 0.14 (0.99)*	–	–	–
E11-18	*5.27 ± 0.11 (0.81)*	*6.33 ± 0.14 (0.99)*	5.21 ± 0.14 (0.39)	6.43 ± 0.20 (0.46)	–
E11-19	5.04 ± 0.14 (0.83)	5.94 ± 0.14 (0.93)	–	–	–
Est. erupt. age	**5.30 ± 0.08 (0.82)**	**6.33 ± 0.10 (0.99)**	–	–	–
Prev. studies	–	–	–	–	10 ± 3
Lower Hut					
E11-01	*5.42 ± 0.12 (0.90)*	*6.32 ± 0.14 (0.99)*	5.62 ± 0.16 (0.41)	6.76 ± 0.18 (0.46)	–
E11-16	4.93 ± 0.13 (0.77)	5.76 ± 0.13 (0.90)	–	–	–
E11-17	*5.30 ± 0.11 (0.85)*	*6.29 ± 0.14 (0.98)*	–	–	–
Est. erupt. age	**5.36 ± 0.08 (0.88)**	**6.31 ± 0.10 (0.99)**	–	–	–
Prev. studies	–	–	2.83 ± 0.24 (0.69)[d]	3.59 ± 0.28 (0.91)[d]	11 ± 2
Tramways					
E11-07	*5.55 ± 0.12 (0.81)*	*6.62 ± 0.15 (1.04)*	5.44 ± 0.17 (0.44)	6.67 ± 0.20 (0.46)	–
E11-14	5.27 ± 0.11 (0.81)	6.19 ± 0.14 (0.97)	–	–	–
E11-15	4.82 ± 0.11 (0.77)	5.71 ± 0.13 (0.89)	–	–	–
Est. erupt. age	**5.55 ± 0.12 (0.81)**	**6.62 ± 0.15 (1.04)**	–	–	–
Prev. studies	–	–	–	–	9 ± 1
Lower Ice Tower Ridge					
E11-22	*6.76 ± 0.15 (0.99)*	*8.07 ± 0.18 (1.26)*	–	–	–
E11-25	*6.57 ± 0.16 (1.09)*	*7.81 ± 0.18 (1.22)*	6.50 ± 0.25 (0.57)	7.93 ± 0.33 (0.60)	–
Est. erupt. age	**6.67 ± 0.11 (1.04)**	**7.94 ± 0.13 (1.24)**	–	–	–
Prev. studies	–	–	3.60 ± 0.27 (0.89)[d]	4.50 ± 0.35 (1.15)[d]	9 ± 4
Southeast					
E11-11	*6.90 ± 0.14 (1.23)*	*8.22 ± 0.19 (1.29)*	–	–	–
E11-29	*6.91 ± 0.15 (1.11)*	*8.24 ± 0.19 (1.29)*	–	–	–
E11-30	*6.75 ± 0.15 (1.03)*	*8.02 ± 0.18 (1.25)*	–	–	–
Est. erupt. age	**6.85 ± 0.08 (1.13)**	**8.16 ± 0.11 (1.28)**	–	–	–
Prev. studies	–	–	–	–	12 ± 2
Northeast					
E11-02	*7.14 ± 0.14 (1.15)*	*8.42 ± 0.19 (1.32)*	6.95 ± 0.16 (0.50)	8.40 ± 0.21 (0.57)	–
E11-02(ol)	5.95 ± 0.13 (0.87)	7.00 ± 0.16 (1.10)	–	–	–
E11-26	*6.86 ± 0.15 (1.03)*	*8.15 ± 0.18 (1.27)*	–	–	–
E11-27	6.70 ± 0.13 (1.20)	8.00 ± 0.18 (1.25)	–	–	–
Est. erupt. age	**7.01 ± 0.11 (1.09)**	**8.28 ± 0.13 (1.30)**	–	–	–
Prev. studies	–	–	3.92 ± 0.37 (0.81)[d]	4.89 ± 0.40 (1.26)[d]	13 ± 1
Upper Ice Tower Ridge					
E11-21	*7.47 ± 0.16 (1.04)*	*8.96 ± 0.20 (1.40)*	–	–	–
E11-23	7.00 ± 0.14 (1.23)	8.36 ± 0.19 (1.31)	6.75 ± 0.19 (0.52)	8.30 ± 0.25 (0.58)	–
Est. erupt. age	**7.47 ± 0.16 (1.04)**	**8.96 ± 0.20 (1.40)**	–	–	–
Prev. studies	–	–	–	–	4 ± 2
South					
E11-10	7.99 ± 0.18 (1.31)	9.74 ± 0.23 (1.52)	7.41 ± 0.22 (0.55)	9.23 ± 0.31 (0.66)	–
E11-28	*8.50 ± 0.19 (1.53)*	*10.34 ± 0.24 (1.62)*	–	–	–
Est. erupt. age	**8.50 ± 0.19 (1.53)**	**10.34 ± 0.24 (1.62)**	–	–	–
Prev. studies	–	–	–	–	6 ± 1
Young Pre-caldera					
E11-04	18.64 ± 0.42 (3.09)	22.19 ± 0.51 (3.47)	17.95 ± 0.45 (1.51)	21.97 ± 0.55 (1.53)	–
Prev. studies	–	–	–	–	23 ± 6
West					
E11-12	27.61 ± 0.63 (4.58)	32.08 ± 0.73 (5.02)	–	–	–
Old Pre-caldera					
E11-31	74.94 ± 1.71 (12.27)	88.16 ± 2.01 (13.80)	–	–	–
E11-31(ol)	71.52 ± 1.64 (11.79)	84.15 ± 1.91 (13.17)	–	–	–
Prev. studies	–	–	–	–	86 ± 8

Exposure ages are reported with both analytical and total uncertainties (total uncertainty is in parentheses). Uncertainties are calculated as described in text and reported at 1σ. The estimated eruption age ("est. erupt. age"), shown in bold, is calculated for each post-caldera lava flow as the error-weighted mean of the *italicized* ages in the flow, which are the oldest ^{3}He ages with overlapping 1σ analytical uncertainties. Helium-3 ages not used to calculate the estimated eruption age for each flow are assumed to be skewed young due to environmental factors such as snow cover and erosion (see sections 5.4 and 5.7).

[a] Exposure age calculated using the flux-based model from Lifton et al. (2014) to scale cosmogenic production rates.

[b] Exposure age calculated using Lal (1991)/Stone (2000) to scale cosmogenic production rates.

[c] All ^{40}Ar/^{39}Ar ages are from Harpel et al. (2004) except the Northwest and Young Pre-caldera flows, which are from Kelly et al. (2008a). The ^{40}Ar/^{39}Ar ages for the Old Pre-caldera and Young Pre-caldera flows are from samples E93013 (Harpel et al., 2004) and E86003 (Kelly et al., 2008a), which are the closest ^{40}Ar/^{39}Ar sample locations to the exposure ages collected for those flows.

[d] Chlorine-36 ages from Kelly et al. (2008a) are recalculated using CRONUScalc, as described in the text (section 5.6). Analytical age uncertainties incorporate uncertainty of the ^{36}Cl concentration (see Kelly et al., 2008a), Cl concentration (3% of the Cl concentration reported in Kelly et al. (2008a) (Aruscavage and Campbell, 1983)), sample thickness (1 cm), bulk density (0.4 g/cm^{3}), and K_2O, CaO, Fe_2O_3, and TiO_2 concentrations (0.01, 0.06, 0.01, and 0.05 wt%, respectively). Total age uncertainties include analytical uncertainties plus atmospheric pressure (5 hPa) and production rate uncertainties (see Table 6). The original published ages from Kelly et al. (2008a), which were scaled using Lal (1991) and reported with analytical uncertainty, are 6.27 ± 0.28 ka for Lower Ice Tower Ridge flow, 5.02 ± 0.20 ka for Lower Hut flow, and 6.84 ± 0.34 ka for Northeast flow.

the exposure ages. Total uncertainties (1σ) of the ^{3}He ages (14–18%) and ^{36}Cl ages (7–9%) are significantly larger than analytical uncertainties mainly due to large uncertainties of the ^{3}He and ^{36}Cl production rates. The 16% uncertainty calculated for the ^{3}He production rate by Phillips et al. (2015) (Table 6) results in especially large total age uncertainties for ^{3}He and is attributed to "less-than-optimal" data by the authors of that paper and described as "probably not representative of the method." Because ^{3}He and ^{36}Cl ages in this study are concordant with each other and the total age uncertainty of the ^{36}Cl ages is smaller than that of the ^{3}He ages, we use only ^{36}Cl ages for comparison with Ar ages for flows in which ^{36}Cl was measured, which include 9 of the 10 post-caldera flows and the Young Pre-caldera flow (Fig. 7). Of these, ^{36}Cl ages (using LSD scaling) and Ar ages agree within 2σ total uncertainty in five of the post-caldera flows and in the Young Pre-caldera flow. This concordance is more a reflection of the large uncertainties of the Ar ages than of similarity between the Ar and ^{36}Cl ages; in fact, concordant ^{36}Cl and Ar ages differ by as much as 96%. In the two flows bearing Ar and ^{3}He ages but no ^{36}Cl age—the Southeast and Old Pre-caldera flows—the Ar and ^{3}He ages agree within 2σ. However, a hypothetical ^{36}Cl age in concordance with ^{3}He ages in the Southeast flow and having a total uncertainty similar to other ^{36}Cl ages in this study would not be in agreement with the Ar age.

For all flows in which ^{36}Cl and Ar ages do not have overlapping 2σ uncertainties (Southwest, Lower Hut, Tramways, and Northeast), the Ar age is older. Given that Erebus anorthoclase crystals contain up to 30% melt inclusions with high concentrations of magmatic excess ^{40}Ar ($^{40}Ar_E$) (Esser et al., 1997), we suspect the older Ar ages are overestimated due to incomplete removal of $^{40}Ar_E$ prior to ^{40}Ar/^{39}Ar analysis. Because the radiogenic ^{40}Ar content of the samples is so low due to their young ages, a small amount of unremoved $^{40}Ar_E$ would significantly affect apparent ages. Concordance of exposure ages and Ar ages in the pre-caldera samples within *analytical* uncertainty supports this explanation, since trace amounts of residual $^{40}Ar_E$ would have a lesser effect on the apparent age of an older sample (note that agreement of the ^{3}He age of sample E11-31 (74.94 ± 1.71 ka) from the Old Pre-caldera flow with the Ar age of the nearest Ar-dated sample (86 ± 8 ka, from Harpel et al., 2004) improves when we consider that the E11-31 surface has probably been eroded (see section 5.4)).

The conclusions of this section change slightly if we use St ages rather than LSD ages. Comparing St-scaled ^{36}Cl ages to Ar ages, four flows do not have overlapping 2σ uncertainties: Northwest, Southwest, Northeast, and Upper Ice Tower Ridge. In two of those flows (Northwest and Upper Ice Tower Ridge) the Ar age is younger than the ^{36}Cl age. Underestimation of Ar ages in samples with extremely low radiogenic ^{40}Ar content can result from precipitation of the K-bearing phase elpasolite onto the mineral grains when the samples were etched in HF to remove melt inclusions (B. McIntosh, pers. comm.), or from overestimation of atmospheric Ar concentrations in blanks. Alternatively, this could be an indication that LSD scaling is more accurate than St scaling or that both the ^{36}Cl and ^{3}He production rates are underestimated.

5.6. Comparison of new exposure ages and published ^{36}Cl ages

Kelly et al. (2008a) measured ^{36}Cl ages in whole rock (phonolite) samples for the Lower Ice Tower Ridge, Lower Hut, and Northeast flows. For comparison with ages determined in this study, we recalculate the Kelly et al. (2008a) ^{36}Cl ages in CRONUScalc using LSD scaling, production rates from Marrero et al. (2015b), and ERA-40 atmospheric pressure. We assume zero topographic shielding, sample thickness of 5 cm, sample bulk density of 1.8 g/cm^{3}, pore H_2O content of 0%, analytical H_2O content of 1.5 wt%, no erosion, and no snow cover. All other data come from the original paper. Analytical and total age uncertainties are calculated as described in Table 7, footnote d. The revised ages, referred to here as $^{36}Cl_{Kelly,rev}$ ages and reported with 1σ analytical and total uncertainties (total uncertainty in parenthesis), are 3.60 ± 0.27 (0.89) ka for Lower Ice Tower Ridge flow, 2.83 ± 0.24 (0.69) ka for Lower Hut flow, and 3.92 ± 0.37 (0.81) ka for Northeast flow (Table 7; the original published ages can be found in footnote d).

The $^{36}Cl_{Kelly,rev}$ ages are 44–50% younger than the ^{36}Cl ages determined on samples from the same flows in this study (Table 7, Fig. 7). We propose that the $^{36}Cl_{Kelly,rev}$ ages are underestimated due to complications related to their high Cl content. Chlorine-36 concentrations of the Kelly et al. (2008a) samples were measured in whole rock with very high Cl concentrations (~1100 ppm), meaning the majority (~80%) of ^{36}Cl was produced by capture of thermal and epithermal neutrons—collectively referred to as low-energy neutrons—by ^{35}Cl. In contrast, production of ^{36}Cl in the anorthoclase samples from this study is dominated by spallation of K and Ca, with only ~2–10% of production coming from low-energy neutrons. Because the compositions of the anorthoclase samples used for ^{36}Cl analysis in this study differ dramatically from the bulk rock samples used by Kelly et al. (2008a), production rate uncertainty is not systematic between the two sample sets and must be taken into account when comparing the their ages. The production rate of ^{36}Cl by spallation of K and Ca has been more precisely calibrated than the production rate of ^{36}Cl from low-energy neutrons, which relies on a complex calculation of the thermal and epithermal neutron fluxes in the vicinity of the sample (Gosse and Phillips, 2001; Marrero et al., 2015b). The uncertainty of the low-energy neutron production rate calculation is reflected in part by the uncertainty of the calibrated parameter $P_f(0)$, the production rate of epithermal neutrons from fast neutrons in the atmosphere at the rock surface (Liu et al., 1994). For the LSD age calculation, we use the value 690 ± 181 neutrons (g air)$^{-1}$ year^{-1} from Marrero et al. (2015b) for $P_f(0)$. Accounting for the large uncertainty of this parameter in the age calculation results in total age uncertainties that are much larger for the Kelly et al. (2008a) samples (21–25%) than for the anorthoclase samples from this study (7–9%). Even larger uncertainties for the $^{36}Cl_{Kelly,rev}$ ages would probably be more realistic since the uncertainty of $P_f(0)$ does not account for error related to bulk rock composition, which directly affects the low-energy neutron flux in the sample (Gosse and Phillips, 2001).

Additional error in the production rate of ^{36}Cl by low-energy neutron capture may be related to the effects of surrounding snow cover on low-energy neutron fluxes. Phillips et al. (2001) and Zweck et al. (2013) have shown theoretically that an abundance of hydrogen within, on, or near a sample can decrease both the epithermal and thermal neutron fluxes in the sample. The effects of near-surface water and snow on low-energy neutron fluxes are not limited to the immediate vicinity of the water or snow but may extend over 100 m into the atmosphere due to the decameter-to-hectometer scale lengths of the mean free paths of thermal and epithermal neutrons in air (e.g., Hendrick and Edge, 1966; O'Brien et al., 1978; Masarik et al., 2007). Zweck et al. (2013) used modeled fluxes to show that snow cover can substantially alter cosmogenic production rates in a sample that is many meters away from the snow. Since most of the Erebus summit plateau is covered in deep snow and ice year-round, it is plausible that the fluxes of low-energy neutrons in surface rocks throughout much or all of the caldera are significantly lower than fluxes predicted based on dry rock. The rate of ^{36}Cl production from low-energy neutrons would then be overestimated and the exposure age underestimated in samples with high Cl content, such as those from Kelly et al. (2008a), whereas the ages of samples with low Cl content would barely be affected.

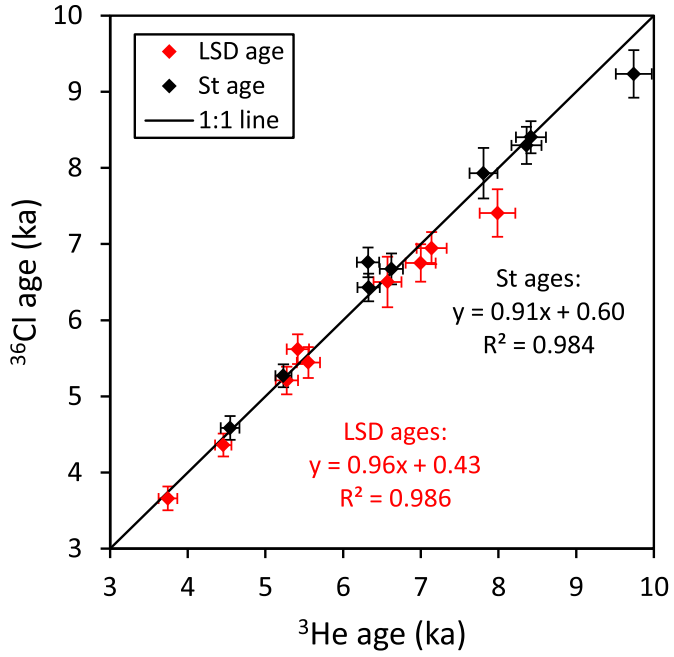

Fig. 5. Comparison of clinopyroxene ^{3}He and anorthoclase ^{36}Cl ages determined in the same samples using the Lifton et al. (2014) (LSD) and Lal (1991)/Stone (2000) (St) methods to calculate production rates. Error bars represent 1σ analytical uncertainty. Sample E11-04 (~17.5 ka LSD age) was also dated using both techniques but is not plotted or included in the linear regression equation or correlation coefficient for each dataset.

Another possible cause of underestimation of the $^{36}Cl_{Kelly,rev}$ ages is overestimation of the nucleogenic ^{36}Cl content of the samples, which is subtracted from the measured ^{36}Cl concentration prior to calculating an exposure age. Nucleogenic ^{36}Cl is produced when neutrons released from light nuclei by (α,n) reactions and from heavy nuclei (primarily ^{238}U) by spontaneous fission are thermalized and captured by ^{35}Cl (Lal, 1987). The primary source of α-particles is the decay of uranium and thorium in the bulk rock matrix, both of which are abundant in Erebus lavas (U = ~6–7 ppm, Th = ~21–22 ppm; Table 5). Exposure ages in this study and in Kelly et al. (2008a) were calculated assuming nucleogenic ^{36}Cl was in secular equilibrium with U and Th in the lava at the time of eruption and has remained at this concentration ever since. Such an assumption would result in age underestimation for young volcanic rocks with high Cl, U, and Th if some or all of the nucleogenic ^{36}Cl accumulated in the melt during residence in the crust was lost prior to or during eruption (Marrero et al., 2015b). In one of the only studies that has addressed this problem, Schimmelpfennig et al. (2009) tested for "magmatic" ^{36}Cl in a fully shielded <400-year-old trachybasalt sample with ~1100 ppm Cl, 2.8 ppm U, and 10.1 ppm Th and determined a ^{36}Cl concentration well below the concentration that would be in secular equilibrium with U and Th in the melt.

If we assume that the nucleogenic ^{36}Cl concentration in all Erebus samples was zero at the time of eruption, the $^{36}Cl_{Kelly,rev}$ ages and 1σ analytical and total age uncertainties become 4.88 ± 0.31 (1.17) ka for the Lower Ice Tower Ridge flow, 4.20 ± 0.21 (0.82) ka for the Lower Hut flow, and 5.23 ± 0.34 (1.01) ka for the Northeast flow, whereas the ^{36}Cl exposure ages from this study increase by 0.2–3.4%. Calculated this way, the $^{36}Cl_{Kelly,rev}$ ages are "only" 25–26% younger than ^{36}Cl ages from this study and agree well within 2σ total uncertainty. At present it is unknown which assumption regarding nucleogenic ^{36}Cl content is most accurate (Marrero et al., 2015b).

In another comparison of exposure ages determined for high Cl and low Cl samples from the same location, Schimmelpfennig et al. (2009) reported ages 30% older in the high Cl samples—the opposite of the trend seen in this study. While we can only speculate on why the age discrepancy between high and low Cl samples revealed by this study is the opposite of that seen by Schimmelpfennig et al. (2009) (possible factors include the use of different values for $P_f(0)$, different snow effects, different erosion histories, and different assumptions regarding nucleogenic ^{36}Cl), we draw the same conclusion as Schimmelpfennig et al.: high Cl samples should be avoided for ^{36}Cl exposure age studies whenever possible.

Table 8
Major element concentrations (wt%) and theoretical compositionally based ^{3}He production rates (atoms/g/a) of clinopyroxene and olivine phenocrysts in samples E11-02, E11-05, and E11-31.

	Si	Al	Fe	Mg	Ca	O	$P_{sp,^3He}(0)$
Clinopyroxene							
E11-02	23.80	1.47	7.68	7.18	15.16	42.30	100.82
E11-05	23.79	1.49	7.43	7.24	15.16	42.29	100.79
E11-31	23.63	1.58	7.16	7.42	15.05	42.20	100.63
Olivine							
E11-02(ol)	16.17	–	30.20	14.73	0.33	37.41	93.43
E11-05(ol)	16.35	–	29.91	15.01	0.33	37.71	94.20
E11-31(ol)	16.48	–	28.23	16.06	0.31	37.97	95.18

$P_{sp,^3He}(0)$ is the theoretical production rate of ^{3}He by spallation of Si, Al, Fe, Mg, Ca, and O predicted by the ^{3}He production rate equation in Masarik (2002). Major element concentrations are averages of all electron microprobe analyses done on each sample. Complete electron microprobe results can be found in Supplement B.

5.7. Eruption chronology of the post-caldera flows

We calculate the estimated eruption age of each of the 10 post-caldera lava flows as the error-weighted mean of the oldest ^{3}He exposure ages that have overlapping 1σ analytical uncertainties (Table 7, Fig. 4). Although the narrow age range observed within most of the flows indicates that snow cover has had only a minor effect on most of the exposure ages, age underestimation due to occasional snow cover still serves as the best explanation for why multiple ^{3}He ages scatter outside of analytical uncertainty in some flows (see section 5.4). Alternatively, there are very few ways in which a ^{3}He exposure age could be overestimated besides production rate or scaling errors, which would be systematic and have little effect on relative ages. The oldest exposure ages in each flow therefore provide the best estimation of the eruption age of the flow. We exclude ^{36}Cl ages from the determination of estimated eruption ages since only one per lava flow was determined.

The estimated eruption ages suggest that the post-caldera flows were erupted much closer together in time than previously thought, spanning a total age range of only ~4000 years. The ages are clustered in time rather than evenly spaced, suggesting that multiple eruptions occurred during relatively brief surges of effusive activity separated by ~700-1100-year-long periods of quiescence (Fig. 4). Repose intervals during surges of activity range from 60 to 460 years in length. These numbers are all slightly larger if St ages are used. The sequence of post-caldera lava flow eruptions, based on estimated eruption ages, is described below using LSD ages and 1σ analytical uncertainty. In general, the chronology of the post-caldera effusive eruptions determined using St ages is similar to that based on LSD ages, but older and extended over a slightly longer time range (Fig. 4).

The oldest post-caldera flow identified is South flow, with an estimated eruption age of 8.50 ± 0.19 ka. The flow is small and lies on the southern side of the caldera close to the Main Crater in an

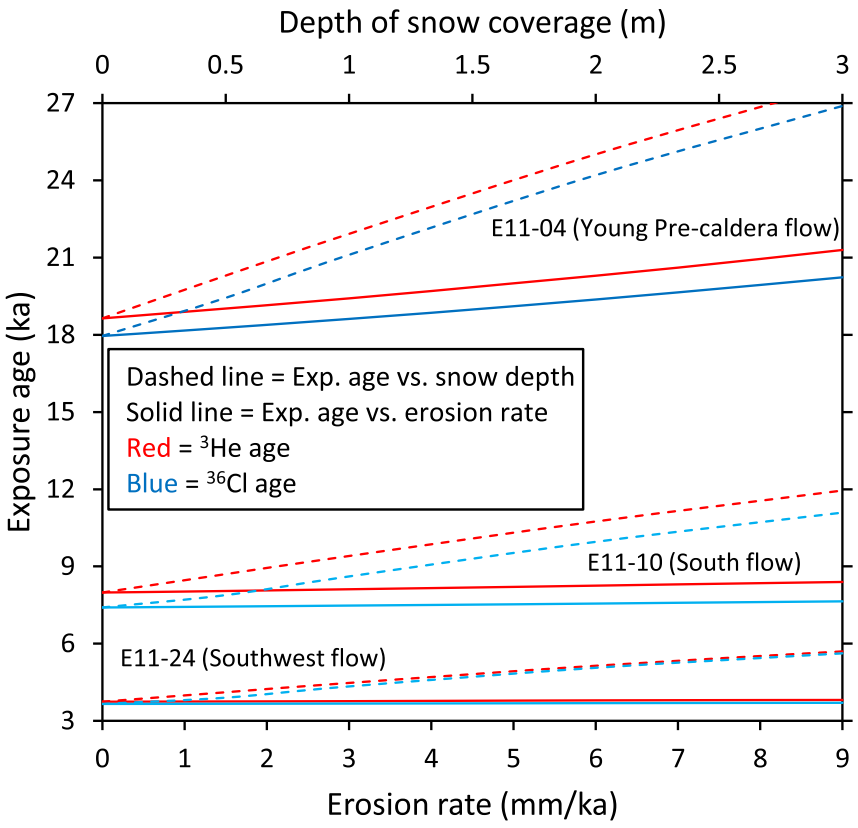

Fig. 6. The effects of snow coverage and erosion on the exposure ages of two samples from post-caldera flows and one from a pre-caldera flow. Only LSD ages are used. Erosion rates are assumed to be constant for the duration of exposure. Exposure ages adjusted for snow cover are calculated assuming a snow density of 0.5 g/cm^3, duration of snow coverage equal to 50% of the sample's exposure age, and an erosion rate of zero. Production rates are corrected for snow cover using equations from Gosse and Phillips (2001) for ^{3}He production and spallogenic ^{36}Cl production and equations from Zweck et al. (2013) for ^{36}Cl production by low-energy neutron capture.

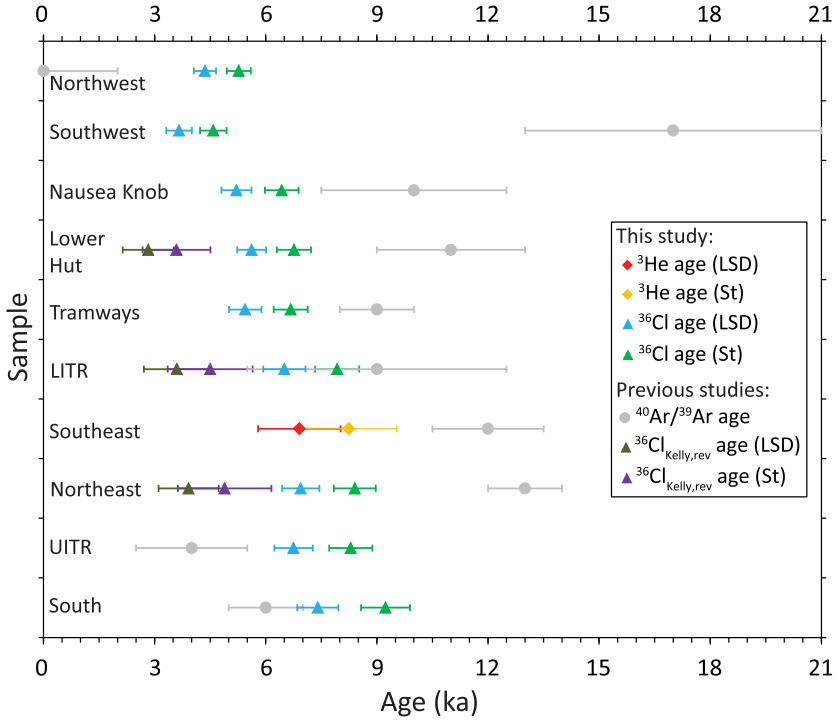

Fig. 7. Exposure ages of the post-caldera lava flows with 1σ total uncertainty versus ^{40}Ar/^{39}Ar ages from Harpel et al. (2004) and Kelly et al. (2008a). Only ^{36}Cl ages are shown for all lava flows except Southeast because the total uncertainty for ^{36}Cl is significantly smaller than for ^{3}He. For the Southeast flow, in which a ^{36}Cl age was not determined, the oldest ^{3}He age is shown instead. The three ^{36}Cl ages from Kelly et al. (2008a), recalculated as described in section 5.6, are also shown with total uncertainty.

area heavily littered by lava bombs. Discordance of the two ^{3}He ages measured here may be explained by short-term burial of the sample locations under bomb debris.

About 1030 years after the eruption of South flow, Upper Ice Tower Ridge (7.47 ± 0.16 ka) was erupted, followed shortly after by the Northeast (7.01 ± 0.11 ka), Southeast (6.85 ± 0.08 ka), and Lower Ice Tower Ridge (6.67 ± 0.11 ka) flows. Ages of the latter three flows are within 2σ analytical uncertainty of each other. Despite their similarity in age, the flows are widely distributed throughout the southern and eastern portions of the caldera.

After an apparent hiatus of ~1120 years, the Tramways (5.55 ± 0.12 ka), Lower Hut (5.36 ± 0.08 ka), and Nausea Knob (5.30 ± 0.08 ka) flows were emplaced in the northern caldera as another pulse of effusive eruptive activity. Ages of the flows produced during this period are again all within 2σ analytical uncertainty of each other, but the flows are much more geographically concentrated than those from the previous set of eruptions. Given their proximity in location and age and the lack of a visible contact between them, Lower Hut and Nausea Knob may actually be the same flow. The Lower Hut flow has by far the largest surface area of any of the summit-area flows, with 42% of the total combined area of all 10 post-caldera flows (see Supplement E). Assuming the summit flows all have similar thicknesses, the highest volume of lava was erupted during this period.

A ~690-year break in activity was followed by the eruption of the final two caldera-filling lava flows: Southwest (4.60 ± 0.11 ka) and Northwest (4.52 ± 0.08 ka). The sample locations in the Southwest flow are low-lying and the likelihood that their exposure ages have been affected by snow coverage is supported by the 19.0% age difference between the oldest and youngest sample. The estimated eruption age given for the Southwest flow therefore has a strong possibility of being underestimated. The probable vent locations for both the Northwest and Southwest flows lie in the southwestern quadrant of the caldera.

No effusive eruptions have occurred on Erebus since the Northwest flow ~4500 years ago. The only subsequent development of the volcanic edifice has been continued growth of the summit cone by the addition of small amounts of pyroclastic material ejected during Strombolian eruptions. The long-term growth rate of the cone can be estimated using the age of the South flow, which has the highest elevation of any lava flow on Erebus. The upper end of the flow lies approximately 50–80 m below the main crater rim. Since the summit cone must have been at least this high when the South flow was erupted at around 8.50 ka, the average rate of cone growth between the eruption of South flow and the present is ~6–9 m/ka.

The combined mapped surface area of the post-caldera flows is approximately 7.44 km^2 (Supplement E). Assuming a uniform thickness of 5 m for all flows, the estimated average eruption rate during the ~4000-year period over which the flows were erupted is 0.01 km^3/ka (the estimate is a minimum because we do not account for lava that flowed past the edge of the summit plateau or pyroclastic material erupted as tephra). This rate is far below the long-term average eruption rate of 1.7 km^3/ka estimated for the entire 1.3-Ma-old Erebus edifice, and even farther from the 4.0 km^3/ka average estimated for the last 250 ka (Esser et al., 2004), illustrating that even the most recent period of effusive activity was part of a long-term quiescent phase on Erebus. For comparison with other currently active polygenetic stratovolcanoes, the average eruption rate of Mt. Sakurajima over the last 14 ka is 1.8 km^3/ka (Crisp, 1984); Mt. Fuji over the last 11 ka is 8 km^3/ka (White et al., 2006); Mt. Etna over the last 439 years is 8.2 km^3/ka (Crisp, 1984); Mt. Vesuvius over the last 313 years is 10.7 km^3/ka (Crisp, 1984); and Mt. Nyamuragira over the last 70 years is 9.2 km^3/ka (Wadge, 1980).

5.8. West flow: new evidence for two caldera collapses

Near the western edge of the caldera at the E11-12 sample location, we presume the existence of a previously unmapped caldera-filling lava flow that is significantly older than the other post-caldera flows sampled in this study. Outcrops in this area were mapped as part of the Northwest flow by Caldwell (1989) and Harpel et al. (2004) and have a field appearance similar to that of outcrops in the Northwest flow. However, we determine a ^{3}He LSD exposure age of 27.61 ± 0.63 ka for E11-12, substantially older than samples E11-05 and E11-13 in the Northwest flow (Table 7). We also note a subtle but distinct difference in clinopyroxene composition, marked primarily by FeO content that is higher than any of the post-caldera flows and similar to the Young Pre-caldera flow (see Fig. B1 in Supplement B), supporting the older age of this sample.

The lava flow containing sample E11-12, here called the West flow, clearly overflows the western caldera rim, meaning it is younger than the collapse of that portion of the caldera. However, eruption of the West flow must also predate collapse of the southwestern portion of the caldera because sample E11-12 is older than the youngest ^{40}Ar/^{39}Ar age of any Young Pre-Caldera flow (21 ± 2 ka; Harpel et al., 2004). Identification of the West flow therefore substantiates the hypothesis, originally proposed by Harpel et al. (2004), that the summit caldera was formed by at least two separate collapse events.

6. Conclusion

We used cosmogenic ^{3}He ages of clinopyroxene and olivine and ^{36}Cl ages of anorthoclase to investigate the chronology of the Erebus summit-area lava flows. The principal conclusions of this study are:

1) Clinopyroxene ^{3}He ages and anorthoclase ^{36}Cl ages determined on the same samples are concordant, with a correlation coefficient of 0.986, implying that the methods used here are robust and the production rates used to calculate ages are internally consistent for the latitude (~77° S) and altitude (~3200–3600 m) of the Erebus summit plateau.
2) Exposure ages calculated using Lal (1991)/Stone (2000) scaling factors are 16–25% older than those calculated using flux-based Lifton et al. (2014) scaling factors, highlighting the magnitude of exposure age uncertainty related to scaling at high latitude and high elevation.
3) Estimated eruption ages calculated for each post-caldera flow based on ^{3}He exposure ages indicate that the flows were erupted during a few closely spaced periods of activity between 4.52 and 8.50 ka (using Lifton et al. (2014) scaling). The average eruption rate over this period is estimated to be 0.01 km^3/ka, far below the average long-term eruption rate of Erebus. Close agreement between multiple ^{3}He ages determined on samples from different areas of the same flows implies that the exposure ages have not been significantly altered by snow coverage.
4) The longest period of repose between eruptions of the post-caldera flows was ~1.1 ka. Given that the youngest flow (Northwest flow) erupted at least 4 ka ago, we consider the most recent effusive eruptive phase to have ended.

Other conclusions are:

5) The ^{3}He/^{4}He ratio of the mantle below Ross Island, as measured in olivine separated from submarine hyaloclastite from the Dry Valley Drilling Project core 3, is 6.91R_a ± 0.08R_a.

6) Large differences (>2σ analytical uncertainty) between ^{3}He ages measured in clinopyroxene and Fe-rich olivine from the same samples highlight the importance of the compositional dependence of ^{3}He production for phases with compositions significantly different than those used to calibrate production rates.
7) Disagreement between the new exposure ages and some of the published ^{40}Ar/^{39}Ar ages for the post-caldera flows (Harpel et al., 2004; Kelly et al., 2008a) is most easily explained by incomplete removal of excess ^{40}Ar in the ^{40}Ar/^{39}Ar samples.
8) Disagreement between the new ^{36}Cl ages measured in anorthoclase and consistently younger ^{36}Cl ages measured by Kelly et al. (2008a) in whole rock samples are best explained by underestimation of the Kelly et al. (2008a) ages due to the high chlorine content of the samples.
9) The West flow, newly identified by its exposure age, is stratigraphically younger than the collapse of the old caldera but has a ^{3}He age older than the youngest of the Young Pre-caldera flows, supporting the proposition that the summit plateau was formed by at least two distinct caldera-forming events.

Acknowledgments

This research was supported by grant ANT-1142083 from the National Science Foundation, Division of Polar Programs. We thank Nels Iverson, Tehnuka Ilanko, and Aaron Curtis for assistance in the field. Antarctic fieldwork would not be possible without the tremendous logistical support from the staff and the civilian contractors working out of McMurdo Station on behalf of the Division of Polar Programs of NSF. We extend special thanks PHI, Inc. and Helicopters New Zealand for the helicopter support. Thanks to the staffs of PRIME Lab at Purdue University and the WHOI isotope geochemistry facility, and Joshua Curtice at WHOI in particular, for analyzing the samples in this study. Finally, this manuscript was greatly improved thanks to insightful feedback from Nelia Dunbar, Bill McIntosh, and two anonymous reviewers.

Appendix A. Supplementary data

Supplementary data related to this article can be found at http://dx.doi.org/10.1016/j.quageo.2015.09.001.

References

Ackert Jr., R.P., Singer, B.S., Guillou, H., Kaplan, M.R., Kurz, M.D., 2003. Long-term cosmogenic ^{3}He production rates from ^{40}Ar/^{39}Ar and K-Ar dated Patagonian lava flows at 47°S. Earth Planet. Sci. Lett. 210, 119–136.
Anslow, F.S., Clark, P.U., Kurz, M.D., Hostetler, S.W., 2010. Geochronology and paleoclimatic implications of the last deglaciation of the Mauna Kea Ice Cap, Hawaii. Earth Planet. Sci. Lett. 297, 234–248.
Aruscavage, P.J., Campbell, E.Y., 1983. An ion-selective electrode method for determination of chlorine in geological materials. Talanta 30, 745–749.
Aster, R., Mah, S., Kyle, P.R., McIntosh, W.C., Dunbar, N.W., Johnson, J., 2003. Very long period oscillations of Mount Erebus Volcano. J. Geophys. Res. 108 (B11), 2522. http://dx.doi.org/10.1029/2002JB002101.
Balco, G., Stone, J.O., Lifton, N.A., Dunai, T.J., 2008. A complete and easily accessible means of calculating surface exposure ages or erosion rates from B-10 and Al-26 measurements. Quat. Geochronol. 3, 174–195. http://dx.doi.org/10.1016/j.quageo.2007.12.001.
Behrendt, J.C., 1999. Crustal and lithospheric structure of the West Antarctic rift system from geophysical investigations – a review. Glob. Planet. Change 23, 25–44.
Borchers, B., Marrero, S., Balco, G., Caffee, M., Goehring, B., Gosse, J., Lifton, N., Nishiizumi, K., Phillips, F., Schaefer, J., Stone, J., 2015. Geological calibration of spallation production rates in the CRONUS-Earth project. Quat. Geochronol. http://dx.doi.org/10.1016/j.quageo.2015.01.009 (in press).
Brenan, J.M., Neroda, E., Lundstrom, C.C., Shaw, H.F., Ryerson, F.J., Phinney, D.L., 1998. Behaviour of boron, beryllium, and lithium during melting and crystallization: constraints from mineral-melt partitioning experiments. Geochim. Cosmochim. Acta 62, 2129–2141.
Caldwell, D.A., 1989. Physical and Geochemical Properties of Summit Flows and Recent Volcanic Ejecta from Mount Erebus, Ross Island, Antarctica. Masters Thesis. New Mexico Tech, Socorro, NM, p. 114.
Caldwell, D.A., Kyle, P.R., 1994. Mineralogy and geochemistry of ejecta erupted from Mount Erebus, Antarctica, between 1972 and 1986. In: Kyle, P.R. (Ed.), Volcanological and Environmental Studies of Mount Erebus, Antarctica. Antarctic Research Series, 66. American Geophysical Union, Washington, D.C, pp. 147–162.
Cerling, T.E., Webb, R.H., Poreda, R.J., Rigby, A.D., Melis, T.S., 1999. Cosmogenic ^{3}He ages and frequency of late Holocene debris flows from Prospect Canyon, Grand Canyon, USA. Geomorphology 27, 93–111.
Crisp, J.A., 1984. Rates of magma emplacement and volcanic output. J. Volcanol. Geotherm. Res. 20, 177–211.
Csatho, B., Schenk, T., Kyle, P., Wilson, T., Krabill, W.B., 2008. Airborne laser swath mapping of the summit of Erebus volcano, Antarctica: applications to geological mapping of a volcano. J. Volcanol. Geotherm. Res. 177, 531–548.
Desilets, D., Zreda, M., Almasi, P.F., Elmore, D., 2006. Determination of cosmogenic ^{36}Cl in rocks by isotope dilution: innovation, validation and error propagation. Chem. Geol. 233, 185.
Dibble, R.R., Kyle, P.R., Skov, M.J., 1994. Volcanic activity and seismicity of Mount Erebus, 1986–1994. Antarct. J. U. S. 29, 11–13.
Dunai, T.J., Stuart, F.M., Pik, R., Burnard, P., Gayer, E., 2007. Production of ^{3}He in crustal rocks by cosmogenic thermal neutrons. Earth Planet. Sci. Lett. 258, 228–236.
Esser, R.P., Kyle, P.R., McIntosh, W.C., 2004. ^{40}Ar/^{39}Ar dating of the eruptive history of Mount Erebus, Antarctica: volcano evolution. Bull. Volcanol. 66, 671–686.
Esser, R.P., McIntosh, W.C., Heizler, M.T., Kyle, P.R., 1997. Excess argon in melt inclusions in zero-age anorthoclase feldspar from Mount Erebus, Antarctica, as revealed by the ^{40}Ar/^{39}Ar method. Geochim. Cosmochim. Acta 61, 3789–3801.
Fenton, C.R., Niedermann, S., 2014. Surface exposure dating of young basalts (1-200 ka) in the San Francisco volcanic field (Arizona, USA) using cosmogenic ^{3}He and ^{21}Ne. Quat. Geochronol. 18, 87–105. http://dx.doi.org/10.1016/j.epsl.2013.10.052.
Fink, D., Vogt, S., Hotchkis, M., 2000. Cross-sections for ^{36}Cl from Ti at Ep = 35–150 MeV: applications to in-situ exposure dating. Nucl. Instrum. Methods Phys. Res. Sect. B 172, 861–866.
Gerst, A., Hort, M., Aster, R.C., Johnson, J.B., Kyle, P.R., 2013. The first second of volcanic eruptions from the Erebus volcano lava lake, Antarctica – Energies, pressures, seismology, and infrasound. J. Geophys. Res. 118, 3318–3340.
Goehring, B.M., Kurz, M.D., Balco, G., Schaefer, J.M., Licciardi, J., Lifton, N., 2010. A reevaluation of in situ cosmogenic ^{3}He production rates. Quat. Geochronol. 5, 410–418. http://dx.doi.org/10.1016/j.quageo.2010.03.001.
Gosse, J.C., Phillips, F.M., 2001. Terrestrial in situ cosmogenic nuclides: theory and application. Quat. Sci. Rev. 20, 1475–1560.
Gupta, S., Zhao, D.P., Rai, S.S., 2009. Seismic imaging of the upper mantle under the Erebus hotspot in Antarctica. Gondwana Res. 16, 109–118.
Hall, J., Wilson, T., Henrys, S., 2007. Structure of the central Terror Rift, western Ross sea, Antarctica. In: Cooper, A.K., Raymond, C.R. (Eds.), Antarctica: a Keystone in a Changing World – online Proceedings of the 10th ISAES: USGS Open-file Report 2007–1047, Research Paper 108.
Harpel, C.J., Kyle, P.R., Esser, R.P., McIntosh, W.C., Caldwell, D.A., 2004. ^{40}Ar/^{39}Ar dating of the eruptive history of Mount Erebus, Antarctica: summit flows, tephra, and caldera collapse. Bull. Volcanol. 66, 687–702.
Hendrick, L.D., Edge, R.D., 1966. Cosmic-ray neutrons near Earth. Phys. Rev. 145, 1023–1025.
Hungerford, J.D., Stone, J.O., Fifield, K., Trusdell, F.A., 2002. Chlorine-36 exposure dating of recent explosive events on Mauna Loa, Hawaii. In: American Geophysical Union Annual Fall Meeting, Abstract #V52B-1288.
Iverson, N.A., Kyle, P.R., Dunbar, N.W., McIntosh, W.C., Pearce, N.J.G., 2014. Eruptive history and magmatic stability of Erebus volcano, Antarctica: insights from englacial tephra. Geochem. Geophys. Geosystems 15, 4180–4202. http://dx.doi.org/10.1002/2014GC005435.
Kelly, P.J., Dunbar, N.W., Kyle, P.R., McIntosh, W.C., 2008a. Refinement of the late quaternary geologic history of Erebus volcano, Antarctica using ^{40}Ar/^{39}Ar and ^{36}Cl age determinations. J. Volcanol. Geotherm. Res. 177, 569–577.
Kelly, P.J., Kyle, P.R., Dunbar, N.W., Sims, K.W.W., 2008b. Geochemistry and mineralogy of the phonolite lava lake, Erebus volcano, Antarctica: 1972–2004 and comparison with older lavas. J. Volcanol. Geotherm. Res. 177, 589–605.
Kurz, M.D., 1986. Cosmogenic helium in a terrestrial igneous rock. Nature 320, 435–439.
Kurz, M.D., Colodner, D., Trull, T.W., Moore, R.B., O'Brien, K., 1990. Cosmic ray exposure dating with in situ produced cosmogenic ^{3}He: results from young Hawaiian lava flows. Earth Planet. Sci. Lett. 97, 177–189.
Kurz, M.D., Curtice, J., Lott, D.E., Solow, A., 2004. Rapid helium isotopic variability in Mauna Kea shield lavas from the Hawaiian Scientific Drilling Project. Geochem. Geophys. Geosystems 5 (4). http://dx.doi.org/10.1029/2002GC000439. AGU. 5, Q04G14.
Kyle, P.R., 1981. Evolution of a basanite phonolite sequence, hut Point Peninsula, Antarctica evidence from Dry Valley Drilling Project Drillholes 1, 2 and 3. J. Petrol. 22, 451–500.
Kyle, P.R., 1990. McMurdo volcanic group-western Ross embayment:introduction. In: LeMasurier, W., Thomson, J. (Eds.), Volcanoes of the Antarctic Plate and Southern Oceans. Antarctic Research Series. American Geophysical Union, Washington, D.C, pp. 18–25.
Kyle, P.R., Moore, J.A., Thirlwall, M.F., 1992. Petrologic evolution of anorthoclase phonolite lavas at Mount Erebus, Ross Island, Andtarctica. J. Petrol. 33, 849–875.

Lal, D., 1987. Production of ^{3}He in terrestrial rocks. Chem. Geol. 66, 89–98.
Lal, D., 1991. Cosmic ray labeling of erosion surfaces: In situ nuclide production rates and erosion models. Earth Planet. Sci. Lett. 104, 424–439.
Licciardi, J., Kurz, M.D., Clark, P., Brook, E., 1999. Calibration of cosmogenic ^{3}He production rates from Holocene lava flows in Oregon, USA, and effects of the Earth's magnetic field. Earth Planet. Sci. Lett. 172, 261–271.
Licciardi, J., Kurz, M., Curtice, J., 2006. Cosmogenic ^{3}He production rates from Holocene lava flows in Iceland. Earth Planet. Sci. Lett. 246, 251–264.
Lifton, N., Bieber, J., Clem, J., Duldig, M., Evenson, P., Humble, J., Pyle, R., 2005. Addressing solar modulation and long-term uncertainties in scaling secondary cosmic rays for in situ cosmogenic nuclide applications. Earth Planet. Sci. Lett. 239, 140–161.
Lifton, N., Sato, T., Dunai, T.J., 2014. Scaling in situ cosmogenic nuclide production rates using analytical approximations to atmospheric cosmic-ray fluxes. Earth Planet. Sci. Lett. 386, 149–160. http://dx.doi.org/10.1016/j.epsl.2013.10.052.
Liu, B., Phillips, F.M., Fabryka-Martin, J.T., Fowler, M.M., Stone, W.D., 1994. Cosmogenic ^{36}Cl accumulation in unstable landforms 1. Effects of the thermal neutron distribution. Water Resour. Res. 30, 3115–3125.
Marrero, S.M., 2012. Calibration of Cosmogenic Chlorine-36. Dissertation. New Mexico Institute of Mining and Technology, USA. http://www.ees.nmt.edu/outside/alumni/papers/2012d_marrero_s.pdf.
Marrero, S.M., Phillips, F., Borchers, B., Lifton, N., Aumer, R., Balco, G., 2015a. Cosmogenic nuclide systematics and the CRONUScalc program. Quat. Geochronol. Accept. Pending Revis. (in press).
Marrero, S.M., Phillips, F.M., Caffee, M., Gosse, J., 2015b. CRONUS-Earth cosmogenic ^{36}Cl calibration. Quat. Geochronol. Accept. Pending Revis.
Masarik, J., 2002. Numerical simulation of in-situ produced cosmogenic nuclides. Geochim. Cosmochim. Acta 66, A491.
Masarik, J., Beer, J., 1999. Simulation of particle fluxes and cosmogenic nuclide production in the Earth's atmosphere. J. Geophys. Res. 104 D, 12099–12111.
Masarik, J., Reedy, R.C., 1995. Terrestrial cosmogenic-nuclide production systematics calculated from numerical simulations. Earth Planet. Sci. Lett. 136, 381–395.
Masarik, J., Kim, K.J., Reedy, R.C., 2007. Numerical simulations of in situ production of terrestrial cosmogenic nuclides. Nucl. Instrum. Methods Phys. Res. Sect. B 259, 642–645.
Niedermann, S., 2002. Cosmic-ray-produced noble gases in terrestrial rocks: dating tools for surface processes. In: Porcelli, D., Ballentine, C.J., Wieler, R. (Eds.), Noble gases in Geochemistry and Cosmochemistry. Reviews in Mineralogy and Geochemistry, vol. 47, pp. 731–784.
O'Brien, K., Sandmeier, H.A., Hansen, G.E., 1978. Cosmic ray induced neutron background sources and fluxes for geometries of air over water, ground, iron and aluminium. J. Geophys. Res. 83, 114–120.
Oppenheimer, C., Kyle, P., 2008. Volcanology of Erebus volcano, Antarctica. J. Volcanol. Geotherm. Res. 177, v–vii.
Oppenheimer, C., Moretti, R., Kyle, P.R., Eschenbacher, A., Lowenstern, J.B., Hervig, R.L., Dunbar, N.W., 2011. Mantle to surface degassing of alkalic magmas at Erebus volcano, Antarctica. Earth Planet. Sci. Lett. 306, 261–271.
Phillips, F., Stone, W.D., Fabryka-Martin, J., 2001. An improved approach to calculating low-energy cosmic-ray neutron fluxes near the land/atmosphere interface. Chem. Geol. 175, 689–701.
Phillips, F.M., Argento, D.C., Balco, G., Caffee, M.W., Clem, J., Dunai, T., Finkel, R., Goehring, B., Gosse, J.C., Hudson, A., Jull, A.J.T., Kelly, M., Kurz, M.D., Lal, D., Lifton, N., Marrero, S.M., Nishiizumi, K., Reedy, R., Schaefer, J., Stone, J.O.H., Swanson, T., Zreda, M.G., 2015. The CRONUS-Earth project: a synthesis. Quat. Geochron (in press).
Rilling, S., Mukasa, S., Wilson, T., Lawver, L., Hall, C., 2009. New determinations of ^{40}Ar/^{39}Ar isotopic ages and flow volumes for Cenozoic volcanism in the Terror Rift, Ross Sea, Antarctica. J. Geophys. Res. 114, B12207.
Schimmelpfennig, I., Benedetti, L., Finkel, R., Pik, R., Blard, P.-H., Bourlès, D., Burnard, P., Williams, A., 2009. Sources of in-situ ^{36}Cl in basaltic rocks. Implications for calibration of production rates. Quat. Geochronol. 4, 441–461. http://dx.doi.org/10.1016/j.quageo.2009.06.003.
Sims, K.W.W., Blichert-Toft, J., Kyle, P.R., Pichat, S., Gauthier, P., Blusztajin, J., Kelly, P., Ball, L., Graham, L., 2008. A Sr, Nd, Hf, and Pb isotope perspective on the genesis and long-term evolution of alkaline magmas from Erebus volcano, Antarctica. J. Volcanol. Geotherm. Res. 177, 606–618.
Steinhilber, F., Abreu, J., Beer, J., 2008. Solar modulation during the Holocene. Astrophys. Space Sci. Trans. 4, 1–6.
Stone, J.O., 2000. Air pressure and cosmogenic isotope production. J. Geophys. Res. 105, 23753–23760.
Stone, J.O., 2005. Terrestrial chlorine-36 production from spallation of iron. In: Abstract of 10th International Conference on Accelerator Mass Spectrometry. Berkeley, California.
Uppala, S.M., Kållberg, P.W., Simmons, A.J., Andrae, U., da Costa Bechtold, V., Fiorino, M., Gibson, J.K., Haseler, J., Hernandez, A., Kelly, G.A., Li, X., Onogi, K., Saarinen, S., Sokka, N., Allan, R.P., Andersson, E., Arpe, K., Balmaseda, M.A., Beljaars, A.C.M., van de Berg, L., Bidlot, J., Bormann, N., Caires, S., Chevallier, F., Dethof, A., Dragosavac, M., Fisher, M., Fuentes, M., Hagemann, S., Hólm, E., Hoskins, B.J., Isaksen, L., Janssen, P.A.E.M., Jenne, R., McNally, A.P., Mahfouf, J.-F., Morcrette, J.-J., Rayner, N.A., Saunders, R.W., Simon, P., Sterl, A., Trenberth, K.E., Untch, A., Vasiljevic, D., Viterbo, P., Woollen, J., 2005. The ERA-40 re-analysis. Q. J. R. Meteorol. Soc. 131, 2961–3012.
Usoskin, I., Solanki, S., Kovaltsov, G., 2007. Grand minima and maxima of solar activity: new observational constraints. Astron. Astrophys. 471, 309–310.
Wadge, G., 1980. Output rate of magma from active central volcanoes. Nature 288, 253–255.
White, S.M., Crisp, J.A., Spera, F.J., 2006. Long-term volumetric eruption rates and magma budgets. Geochem. Geophys. Geosystems 7 (3), 1–20. http://dx.doi.org/10.1029/2005GC001002. AGU. 7, Q03010.
Zreda, M.G., 1994. Development and Calibration of the Cosmogenic ^{36}Cl Surface Exposure Dating Method and its Application to the Chronology of Late Quaternary Glaciations. Dissertation. New Mexico Tech, Socorro, NM, p. 318.
Zweck, C., Zreda, M.G., Desilets, D., 2013. Snow shielding factors for cosmogenic nuclide dating inferred from Monte Carlo neutron transport simulations. Earth Planet. Sci. Lett. 379, 64–71. http://dx.doi.org/10.1016/j.epsl.2013.07.023.